Optical modulators

3

Graham Reed[1], *David Thomson*[1], *Weiwei Zhang*[1], *Frederic Gardes*[1], *Lorenzo Mastronardi*[1], *Ke Li*[1], *Shinji Matsuo*[2], *Shigeru Kanazawa*[2], *Laurent Vivien*[3], *Christian Lafforgue*[3], *John E. Bowers*[4], *Christian Koos*[5], *Marco Romagnoli*[6], *Marko Lončar*[7], *Mian Zhang*[7], *Stefan Abel*[8] *and Ling Liao*[9]
[1]Optoelectronics Research Centre, University of Southampton, Southampton, United Kingdom, [2]NTT Device Technology Labs, NTT corporation, Atsugi-shi, Kanagawa, Japan, [3]Centre de Nanosciences et de Nanotechnologies, CNRS, Université Paris-Saclay, Palaiseau, France, [4]Department of Electrical and Computer Engineering, University of California, Santa Barbara, CA, United States, [5]Institute of Photonics and Quantum Electronics (IPQ), Karlsruhe Institute of Technology (KIT), Engesserstr. 5, Karlsruhe, Germany, [6]CNIT, Photonics Networks and Technologies Laboratory, Pisa, Italy, [7]John A. Paulson School of Engineering and Applied Sciences, Harvard University, Cambridge, MA, United States, [8]Lumiphase AG, Kilchberg, Switzerland, [9]Photonic Integration, Silicon Photonics Product Division, Intel Corporation, Santa Clara, CA, United States

3.1 Introduction

This chapter discusses the possible mechanisms for optical modulation, technology platforms, the current state of the art, and the prospects for the future progression of optical modulators, all for applications in data communication applications. Due to the ever-increasing demand for data, the transition from electrical to optical interconnect within data centers is inevitable. Due to their inclusion in more traditional optical communications applications, III−V material-based modulators were obvious candidates for short-reach interconnect, but the phenomenal rise of silicon photonics has meant that silicon-based modulators are now extensively deployed within such applications, and a brief review of the emergence of silicon-based modulators serves as a useful introduction to silicon photonics technology. Later in this chapter, we will see that recent alternatives are emerging, where other materials are introduced onto the silicon photonics platform as innovative ways of developing modulators that have the best attributes of the new materials but remain compatible with silicon photonics. The chapter begins with a discussion of modulation mechanisms, key modulator parameters, and figures of merit (FoM).

Integrated Photonics for Data Communication Applications. DOI: https://doi.org/10.1016/B978-0-323-91224-2.00011-4

3.2 Modulation mechanisms

Optical modulation is obtained by converting an electrical signal into an optical signal. This can be achieved either by directly modulating the current of the light source or by an electro-optic (EO) effect via an optical modulator (Fig. 3.1).

EO effects can be separated into two main categories: *electro-absorption* (EA) and *electro-refraction effects*. The primary electric field effects that are traditionally used in semiconductor materials for causing either EA or electro-refraction are the plasma dispersion effect, the Pockels effect, the Kerr effect, the Franz–Keldysh effect (FKE), and the Quantum-confined stark effect (QCSE). The performance of both EA and electro-refraction optical modulators can be evaluated by defining performance metrics such as extinction ratio (ER), insertion loss (IL), optical bandwidth, footprint, and power consumption. The ER is defined by the ratio between the "on" and "off" states:

$$\mathrm{ER} = 10.\log\left(\frac{I_{\max}}{I_{\min}}\right)$$

where I_{max} is the intensity of the on state and I_{min} is the intensity of the off state (Fig. 3.1).

A large ER is required for long-distance communication, low bit error rates, and high receiver sensitivity. The IL is the optical loss induced by the optical modulator and is defined by:

$$\mathrm{IL} = 10.\log\left(\frac{I_{\max}}{I_0}\right)$$

with I_0 being the optical intensity at the modulator input (Fig. 3.1).

The mechanisms responsible for power consumption in a diode-based optical modulator are the charging and discharging of the device capacitance (dynamic dissipation), the "static" dissipation from the absorption of optical power, and the dissipation from photocurrent flow.

In addition to the ER and IL, the −3 dB electro-optical bandwidth (BW_{3dB}), the maximum data rate (bit/s), device compactness and the optical bandwidth

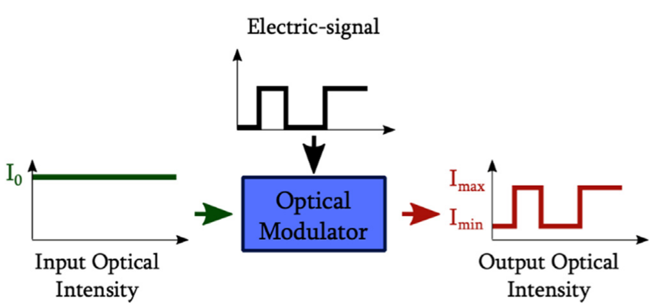

Figure 3.1 Schematic diagram of the principle of an optical modulator, converting an electrical signal into an optical signal.

(or spectral width) referring to the useful operational wavelength range, have also to be determined. More specifically for phase optical modulators (electro-refraction), two additional FoM can be defined: the modulation efficiency ($V_\pi L_\pi$) and the IL for a length, L_π (IL_π). V_π and L_π are the voltage and the length for a pi radian phase change. L_π can be calculated as:

$$L_\pi = \frac{\lambda}{2.\Delta n_{eff}(V_\pi)}$$

where λ is the operating wavelength and Δn_{eff} is the effective index change produced in the modulator under an applied voltage.

The efficiency, $V_\pi L_\pi$, in units of $V \cdot cm$ relates the voltage and length required to obtain a π radian phase shift as defined by:

$$V_\pi L_\pi = \frac{V_\pi \lambda}{2.\Delta n_{eff}(V_\pi)}$$

The lower $V_\pi L_\pi$, the more efficient the modulator.

We have seen that modulation mechanisms are based on the change of refractive index of a material. The most common physical effects associated with electro-refraction modulation are the thermo-optic effect, the plasma dispersion effect, the Pockels effect, and the Kerr effect, while for EA modulation they are the FKE and the QCSE [1].

3.2.1 The thermo-optic effect

The thermo-optic effect is the modification of the real part of the refractive index of the material due to a change in its temperature. This change can be obtained by a Joule effect induced by an electric current. In silicon, this effect is [2]:

$$\Delta n/\Delta T = 1.86 \times 10^{-4}\ K^{-1}$$

Even though this effect is often strong, it is well known to be slow and may require high electrical power to generate heating. In general, it is used as a means to tune the operating point of photonic devices, for example, in Mach−Zehnder interferometers (MZIs) [3] and resonators.

3.2.2 The free-carrier plasma dispersion effect

The free-carrier plasma dispersion (FCPD) effect describes a change in free-carrier concentration in a semiconductor (typically a change in both electrons and holes), leading to a change in refractive index (both real and imaginary). An increase of carriers increases the imaginary refractive index ($\Delta\alpha$: variation of the absorption coefficient) and decreases the real refractive index (Δn). This effect is described by the Drude−Lorentz model [4]:

$$\Delta \text{n} = -\frac{e^2\lambda^2}{8\pi^2 c^2 \varepsilon_0 \text{n}}\left(\frac{\Delta N_e}{m_e} + \frac{\Delta N_h}{m_h}\right)$$
$$\Delta\alpha = \frac{e^3\lambda^2}{4\pi^2 c^3 \varepsilon_0 \text{n}}\left(\frac{\Delta N_e}{m_e^2 \mu_e} + \frac{\Delta N_h}{m_h^2 \mu_h}\right)$$

where e is the charge of the electron; c is the speed of light; λ is the wavelength; n is the refractive index of the unperturbed material; ε_0 is the vacuum permittivity; ΔN_e and ΔN_h are the free-carrier concentrations of electrons and holes respectively; m_e and m_h are the electron and hole relative masses; μ_e and μ_h are the mobilities of electron and holes, respectively. For silicon, Soref and Bennet [5] defined a set of empirical equations from experimental results for the wavelengths of 1.3 and 1.55 μm. For $\lambda = 1.55$ μm, the variations of absorption and refractive index with carrier concentration are shown in Fig. 3.2 and take the following form:

$$\Delta n = -8.8\times 10^{-22}\Delta N_e - 8.5\times 10^{-18}(\Delta N_h)^{0.8}$$
$$\Delta\alpha = 8.5\times 10^{-18}\Delta N_e + 6\times 10^{-18}\Delta N_h$$

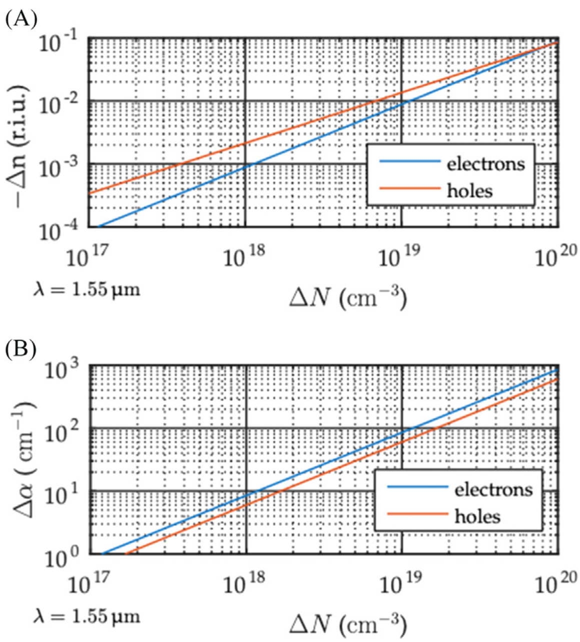

Figure 3.2 Refractive index absorption changes with variation of electron and hole concentrations according to Soref's empirical model [5].

where N_e and N_h are expressed in cm^{-3}, $\Delta\alpha$ in units of cm^{-1}, and Δn in refractive index units.

It can be seen that the variation of hole concentration induces a stronger refractive index change and a weaker absorption change than the variation in electron concentration for carrier concentrations $\Delta N < 8 \times 10^{19}\ cm^{-3}$. The design of Si modulators based on the FCPD effect should take into account these differences to optimize the modulation efficiency and reduce the carrier-induced loss. The modification of electron and hole concentrations in Si is typically carried out by applying a voltage through a diode fabricated in the vicinity of an optical waveguide.

It can also be seen that the EA induced by the FCPD effect is weak [6]. Therefore the FCPD effect is mostly used as an electro-refraction effect, that is, a phase variation. The change in absorption is then limited by design, to minimize loss. The FCPD effect can be achieved through three carrier regimes: injection, accumulation, or depletion of carriers.

- Carrier injection is usually achieved via forward bias of a p-i-n diode leading to current flow through the junction. The intrinsic region is then flooded with carriers (electrons and holes), which induce a refractive index change.
- Carrier depletion is usually exploited via reverse bias of a pn junction. This pn junction induces a small depletion (intrinsic) zone in the vicinity of the junction, that is, a space charge zone. The size of the depletion region increases under reverse bias, sweeping carriers out (depletion), and inducing a variation of refractive index and absorption.
- Carrier accumulation is obtained by employing a MOS-like capacitor. In the Si photonics platform, it is typically composed of a p-doped Si region, an oxide barrier, and an n-doped Si region. When the MOS capacitor is forward biased, charge accumulates at both interfaces of the oxide, holes in the p-doped region and electrons in the n-doped region, inducing a refractive index change close to these interfaces.

FCPD-based optical modulators are fabricated by inserting such electronic structures into Si waveguides. To ensure optimized modulation efficiency, that is, low $V_\pi L_\pi$, waveguide engineering is required to achieve good overlap between the optical mode and the carrier variations. To ensure low IL, care is taken to avoid mode interaction with both doped areas and metallic contacts, and by optimizing the concentrations of the doped regions. The efficiency is linked to the position of all doping regions relative to the waveguide.

Based on the variety of electronic structures to exploit the FCPD effect and the possibility offered by silicon photonics platforms to confine the optical mode, a variety of optical modulators can be then imagined as shown in Fig. 3.3: lateral [7], vertical [8], interleaved [9] structures for carrier injection [10], depletion [7], and accumulation [11]. Even though almost all of them have been experimentally demonstrated, it is obvious that some are more complex to fabricate and integrate with a global circuit, including lasers, modulators, and detectors. However, each has its unique advantages.

3.2.3 Electro-absorption modulation

3.2.3.1 The Franz–Keldysh effect

The FKE occurs in bulk semiconductors. In general, semiconductors absorb photons with energies ($E = hc/\lambda$) higher than the bandgap, shown schematically in

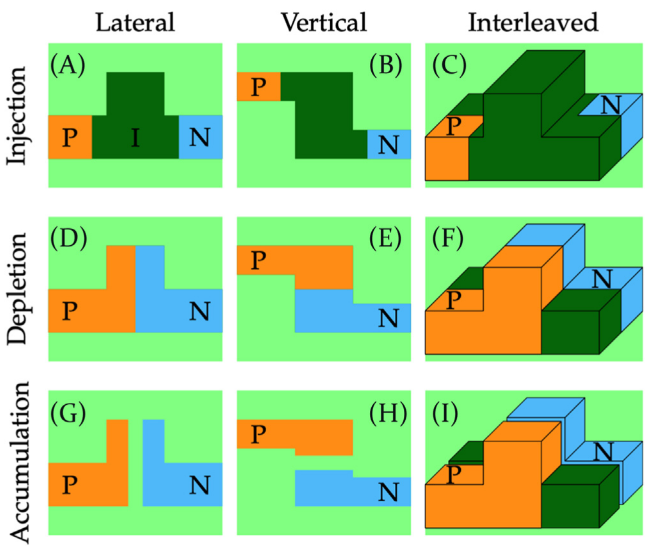

Figure 3.3 Waveguide implementation of modulators based on free-carrier plasma dispersion: (A) lateral carrier injection, (B) vertical carrier injection, (C) interdigitated carrier injection, (D) lateral carrier depletion, (E) vertical carrier depletion, (F) interdigitated carrier depletion, (G) lateral carrier accumulation, (H) vertical carrier accumulation, and (I) interdigitated implementation of carrier accumulation [12,13].

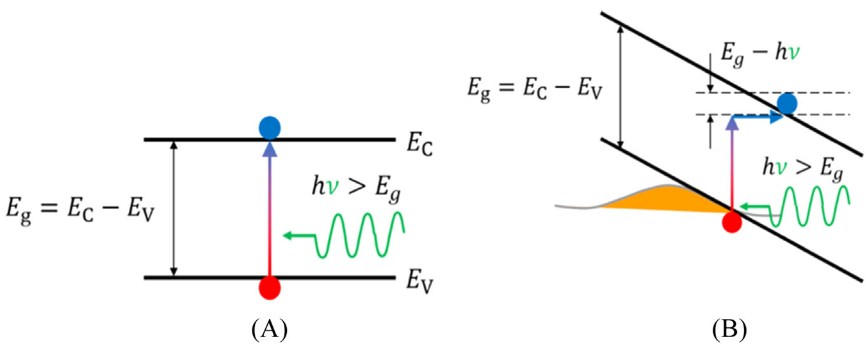

Figure 3.4 Franz–Keldysh effect: (A) photon absorption in equilibrium state, (B) photon absorption under an applied electric field.

Fig. 3.4A. The semiconductor is transparent for photon energies lower than the gap energy (E_g), while it absorbs light for energy higher than the band gap, for example, under an electric field, the energy bands are tilted leading to a penetration of electron and hole wavefunctions into the bandgap, respectively, in the valence and conduction bands, reducing the energy required for a photon to be absorbed by tunneling (Fig. 3.4B). This phenomenon induces a redshift of the absorption spectrum, giving rise to a strong EA effect at photon energies near the gap energy (E_g).

The higher the applied electric field, the greater the electron and hole wavefunction penetration into the energy bandgap, and consequently, the lower the photon energy inducing absorption, and the stronger redshifting. It can also be seen that an electro-refraction effect linked to the EA effect is simultaneously present and is linked via the Kramers−Kronig relations. In silicon the EA due to the FKE (a maximum at $\lambda \approx 1.07\ \mu m$) is weak due to the need for strong phonon-assisted absorption, which is related to the large separation of the indirect and direct bandgap energies. However, in germanium (Ge), this separation is rather low leading to promising characteristics in terms of frequency response, device compactness, and efficiency at a wavelength of about 1.6 μm, corresponding to the direct bandgap energy. Furthermore, the addition of a fraction of Si into the Ge crystal can successfully shift the operational wavelength to 1550 nm [14].

3.2.3.2 The Quantum-confined stark effect

The mechanism of the QCSE is similar to the FKE, that is, a shift toward lower energy of the absorption spectra (longer wavelengths) under an electric field, but in a confined region. The QCSE is found in multiquantum well (MQW) heterostructures. The confinement of electrons and holes within a well, formed by the combination of two direct-like band-gap semiconductors (one for the wells and another for the barriers) enables a discretization of the density of states above the band edge (Fig. 3.5A). This has two main effects: (1) an increase of the gap energy (shift of the absorption edge to the shorter wavelengths), a sharper absorption edge than in bulk material, and (2) a strong Coulomb interaction between the electrons and holes, leading to excitonic effects. The latter induces an additional absorption peak near the absorption edge. As with the FKE, under an electric field, a redshift of the absorption edge occurs due to the modification of both electron and hole

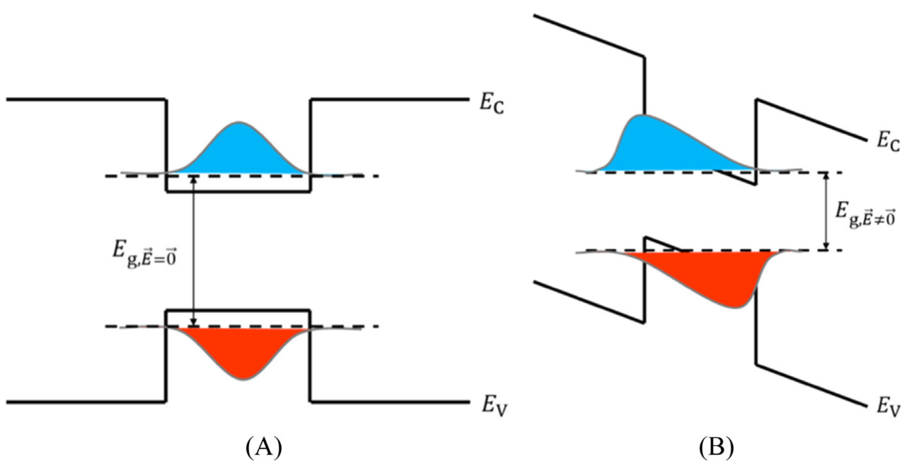

Figure 3.5 Quantum-confined stark effect: quantum well and wavefunction evolutions (A) without an electric field and (B) under an electric field.

wavefunction distributions in the well (Fig. 3.5B) and additionally, a reduction of the excitonic energy contributing to large absorption variation.

Even though III−V semiconductors in QW structures are the material choices due to their direct band-gap nature, Ge-rich SiGe MQW heterostructures have demonstrated promising behavior in terms of efficiency, power consumption, and speed [15,16].

3.2.4 Nonlinear optical effects

Under a high electric field applied to a material, a nonlinear dielectric polarization is created due to the modification of the electronic cloud's center of mass relative to the nucleus. This modification induces a change in refractive index (Δn) as a function of an electric field F:

$$\Delta n \simeq \frac{\chi^{(2)} F}{n} + \frac{3\chi^{(3)} F^2}{2n}$$

where n is the refractive index of the material at the wavelength under consideration. The second-order term related to $\chi^{(2)}$ corresponds to the Pockels effect and consists of the dependence of the refractive index with a static electric field F. The third-order term related to $\chi^{(3)}$ corresponds to the Kerr effect.

3.2.4.1 Pockels effect

The refractive index change induced by the Pockels effect is proportional to electric field. This linear EO effect is largely used in optical communications through ferroelectric materials including lithium niobate (LN) ($LiNbO_3$) [17] and barium titanate ($BaTiO_3$ or BTO) [18]. The absence of a variation of absorption is beneficial for pure phase optical modulation. Such an effect only occurs in noncentrosymmetric materials, and consequently, Si does not exhibit a Pockels effect, unless exposed to material strain that can break its crystal symmetry [19].

3.2.4.2 Kerr effect

The quadratic term in Δn (i.e., the Kerr effect) can also induce nonnegligible refractive index changes in both DC and AC regimes. Indeed, when applying both DC and AC electric fields ($F(t) = F_{DC} + F_{AC} \cdot cos(wt)$), the refractive index change from the Kerr effect can be expressed as:

$$\Delta n = \frac{3\chi^{(3)}}{2n}\left[\left(F_{DC}^2 + \frac{1}{2}F_{AC}^2\right) + 2F_{DC}F_{AC}\cdot\cos(\omega t) + \frac{1}{2}F_{AC}^2\cdot\cos(2\omega t)\right]$$

The term in F^2_{DC} is the DC Kerr effect. An additional static refractive index change arises from the AC component with an amplitude proportional to F^2_{AC}. Furthermore, the AC driving field creates an index variation at double the driving frequency ($2w$) with a quadratic dependence on F_{AC}. Finally, a mixed term proportional to $F_{DC}\,F_{AC}$ induces a refractive index change at the same driving field frequency, which is an electric field-induced second-order nonlinear optical effect, that is, a quasi-$\chi^{(2)}$ effect (a Pockels-like effect).

3.2.4.3 Other effects

Any change in the refractive index or absorption of a material under the effect of an external excitation can be used for light modulation. That is the case for many other approaches as follows:

- Electro-refraction and EA based on 2D materials. Graphene is a good example of such approach (see Section 3.6.3).
- Modulation induced by surface wave excitation [20].
- Micro-opto-electro-mechanical systems [21].
- Phase-change materials for low-speed modulation or switching.

3.3 Historical review

The study of silicon photonics modulators goes back almost to the very beginning of research into silicon photonics. The first modulator based on the plasma dispersion effect was proposed by Soref and Bennett in 1986 [22]. It was a theoretical study of a submicron modulator (cross-sectional dimensions), based in silicon, before the popularity of silicon on insulator (SOI) as a substrate material that is the basis of silicon photonics technology today. Modeling suggested that the modulator would achieve a π radian phase shift over a length of 1 mm, for a corresponding loss of 1 dB. This was a p^{+}-n-n^{+} structure that would activate carrier injection under forward bias. The majority of the early silicon photonics work was based on large multimicron waveguides, and consequently, most early modulator designs (and/or switches) were based on carrier injection (e.g., Refs. [23−26]). A detailed review of this very early work is given in Ref. [27]. By the mid-1990s, almost all modulator work focused on designs in SOI material, whereas some of the earlier work had been based on a doped silicon cladding. Authors were also investigating 3-terminal devices (e.g., Refs. [28,29]), or devices with very deep doping (e.g., Refs. [30,31]) to improve modulation speed and power efficiency, or even to look at new applications such as beam steering. Optimization of both 2-terminal and 3-terminal modulators continued throughout the 1990s and early 2000s, to continue to improve device performance in these multimicron waveguide-based devices, with speed, efficiency, and power consumption still being the focus (e.g., Refs. [32−34]). In 2000 Dainesi et al. [35] produced a new device (Fig. 3.6), also targeting performance optimization. While the performance was modest at 10 MHz, the device was interesting as it included segmented doping regions which would return to popularity in later years. The device was fabricated in a large 10-μm thick silicon guiding layer and based on carrier injection, but this was a time when researchers were just beginning to recognize the high speed-potential of high-speed silicon modulators, which could be achieved by reducing the cross-sectional dimensions of

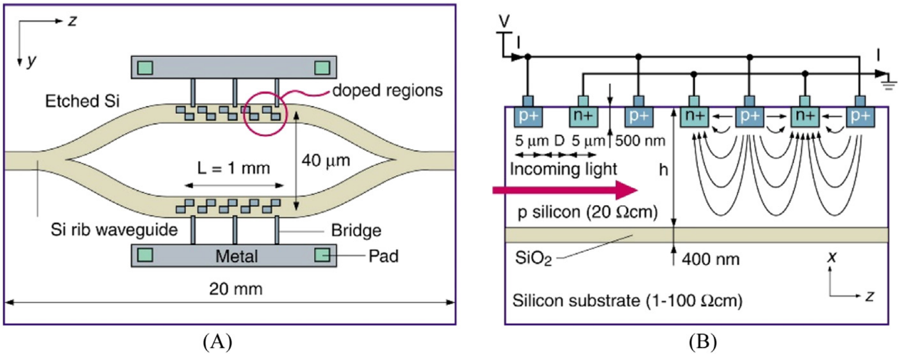

Figure 3.6 Modulator of Dainesi et al., with segmented doping regions from 2000, in (A) plan view, and (B) cross sectional view [35].

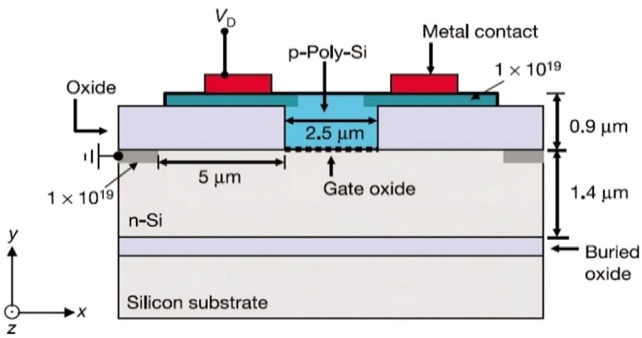

Figure 3.7 The first silicon modulator to operate beyond 1 GHz [35].

the waveguides. Consequently, the typical multimicron devices that were common in the 1980s and 1990s began to give way to smaller devices, toward the submicron devices that dominate today.

The year 2004 was important in the evolution of silicon photonics modulators. In February of 2004, the Intel group published an important breakthrough paper [36], reporting a speed milestone. This was the first experimental device to exceed a bandwidth of 1 GHz, but also the first carrier accumulation-based modulator (also known as a MOSCAP device). The device was demonstrated with a 1 Gb/s data stream. The device is shown in Fig. 3.7 and is notable for high-speed performance despite the overall device thickness exceeding 2 μm. The device was significantly improved the following year [37], to reach data rates of 10 Gb/s at an ER of 3.8 dB.

Also, in 2004, Png et al. [38] designed a range of carrier injection devices predicted to operate from 70 MHz to beyond 1 GHz for the first time. These devices were based on a waveguiding layer of 1.38 μm in thickness. Furthermore, this chapter proposed the use of the preemphasis drive technique to improve the speed to almost 6 GHz. The devices discussed thus far in this introduction have all been phase modulators that realized intensity modulation (IM) via incorporation into an MZI. However, in 2005, Xu et al. [39] very effectively combined a ring resonator structure with a small waveguide to produce a low-power modulator operating at 1.5 Gb/s. This device, however, while being a carrier injection modulator, was based in a much smaller waveguide, with a width of 450 nm, and a height of 250 nm, much more typical of the small waveguides that are common today. The device was later enhanced in speed to 18 Gb/s in 2007 using the preemphasis technique proposed by Png [38]. The attributes of resonant modulators vs interferometric devices such as the MZI will be discussed in more detail later, but it is worth noting in passing that resonant structures typically offer the possibility of smaller footprint than MZIs, at the expense of narrow spectral range and thermal sensitivity. The latter has limited the commercial applications of ring structures, but devices are now starting to emerge from the research laboratory, typically utilizing an electronic feedback circuit to compensate for thermal drift, adding complexity, additional energy consumption, and potentially a need for additional electronic integration. EA modulators (EAMs), on the other hand, also offer a small footprint, potentially without the need for electronic control, although at the price of fabrication complexity. EAMs are discussed in more detail in Section 3.4.3. The trend to smaller waveguides throughout the 2000s opened up the possibility of using depletion of carriers, rather than injection or accumulation, because it became possible to deplete an entire waveguide if it is small enough. Depletion modulators are the most common commercial device available today, and almost the workhorse of silicon photonics transceivers. The first proposal for a depletion modulator in a submicron waveguide was published in 2005 by Gardes et al. [40], an important milestone in silicon modulator development. The device design was based on a horizontal p-n junction across the waveguide (Fig. 3.8) and was

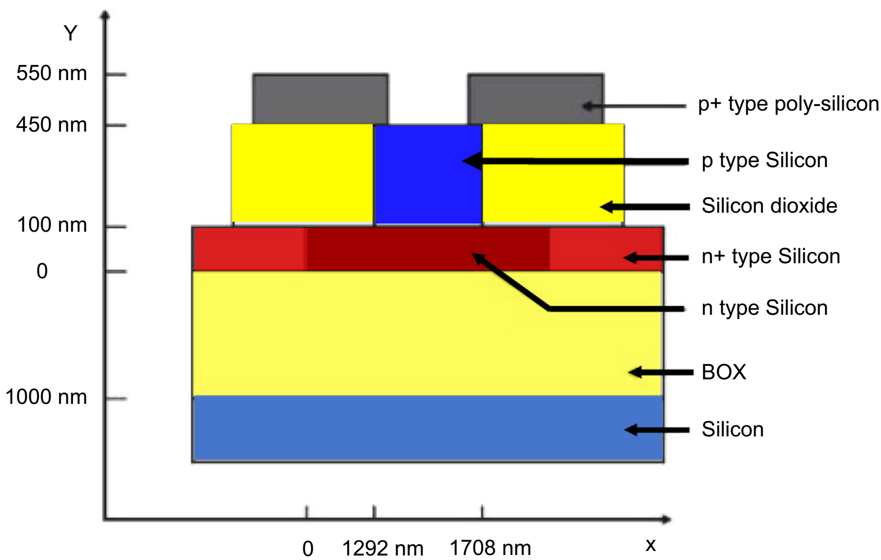

Figure 3.8 The first proposed depletion modulator, now an industry standard device [8].

analyzed via simulation, predicting an unprecedented 50 GHz bandwidth. A series of important results were reported within the next 6 years to take experimentally verified data rates to 30 Gbit/s [41] and 40 Gbit/s [42] in 2007, 40 Gbit/s with high ER in 2011 [43], 40 Gbit/s for transverse electric (TE) and transverse magnetic (TM) polarizations also in 2011 [8], and 50 Gbit/s in 2012 [44].

Since then a plethora of research has been published to increase the data rate of silicon photonics transceivers, while reducing power consumption, integrating with electronic drivers, and utilizing enhanced modulation schemes to improve the overall performance. Today silicon photonics is unrecognizable when compared to the preliminary activities in the late 1980s and early 1990s, and the modulator is perhaps the device that has changed the most, moving from modulation speeds of a few Mbits/s to more than 100 Gbit/s in 2020 [45], at dramatically lower power consumption, and increasing complexity both in terms of integration with other devices, but also in terms of integration with other materials. This chapter discusses these changes, concluding with comments on the outlook for the future.

3.4 Group IV modulators

In the previous section, many of the EO effects used in optical modulators were introduced together with metrics used to assess the performance, such as the ER, IL, 3 dB EO bandwidth, maximum data rate, optical bandwidth, and compactness. The efficiency of the modulator in terms of its voltage and current-length products was also discussed. In this section, more details of the practical implementation of devices based upon these effects using group IV materials are provided, together with demonstrated examples. Another important aspect to consider is the required interfacing electronics, namely, the driver amplifier. As the performance requirements have advanced, it has become increasing important to consider the driver, modulator, and any parasitics from the chosen integration scheme, as a single system to ensure that the highest performance levels are achieved. This is discussed in the last part of this section.

3.4.1 Modulation methods

Depending on the application of the data link that the modulator is serving, either phase or IM may be required. In the previous section, we have seen that the thermo-optic, FCPD, Pockels and Kerr effects are predominantly electro-refractive whereas the FKE and QCSE are predominantly electro-absorptive. Although the FCPD effect is predominantly electro-refractive, it has been the most popular effect used for IM owing largely to the simplicity in forming devices of this type in a silicon waveguide system by using CMOS-like process steps. To achieve IM from electro-refractive effects, a passive optical structure is employed to convert phase modulation. Many structures have been proposed and demonstrated to perform this function that can be split into two categories, interferometric and resonant, the operation of which will be described next as well as in Chapter 5.

3.4.1.1 Interferometric photonic modulators

The most popular structure using the interferometric approach is the MZI as shown in Fig. 3.9. The operation of interferometric modulators is based upon splitting the input light into two paths, performing phase modulation of the light in at least one of the two paths before recombining them into one or more output paths.

When light from the two paths recombines, it will interfere, depending on the relative phase. If in-phase, the light will interfere completely constructively giving a maximum intensity output. If π radians out of phase, it will interfere completely destructively and give a minimum intensity output. If the relative phase is in between these two states, then the intensity will be between the minimum and maximum, following the well-known transfer function as shown in Fig. 3.9.

In this way the phase modulation produced by the phase modulator can be translated into IM. In a perfect interferometer the light is split equally into the two paths, experiences the same propagation losses in each path, and is then recombined. Deviation from this ideal case will cause the minimum level to deviate from zero and increase loss at the maximum level. Ideally, the device will be insensitive to the polarization and the wavelength of light, which may be possible within certain practical operational ranges. The phase of one or both of the arms may be varied. When the phase in both arms is varied, it can be varied in opposition to effectively double the relative phase difference, at the combiner. Using this approach has many advantages, including lower drive power, shorter device length, reduced output chirp, and balanced optical losses. However, it requires double the number of drive signals unless a single-drive push–pull approach is employed [46].

3.4.1.2 Resonant photonic modulators

The most popular structure using the resonant approach to convert phase shift to amplitude modulation is the ring resonator as shown in Fig. 3.10. Resonant modulators work by incorporating the phase modulator into the resonant structure so as to enable modulation of the optical path length, and therefore the wavelength at which

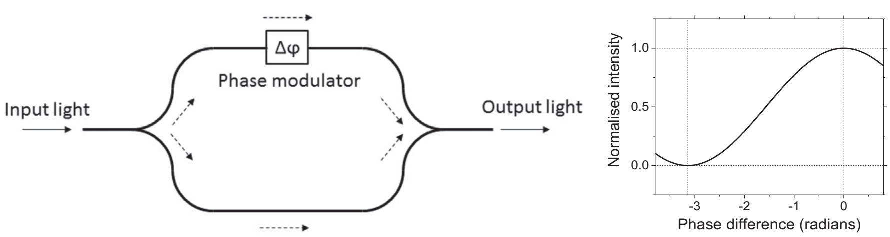

Figure 3.9 Diagram of a Mach–Zehnder interferometer-based modulator and transfer function.

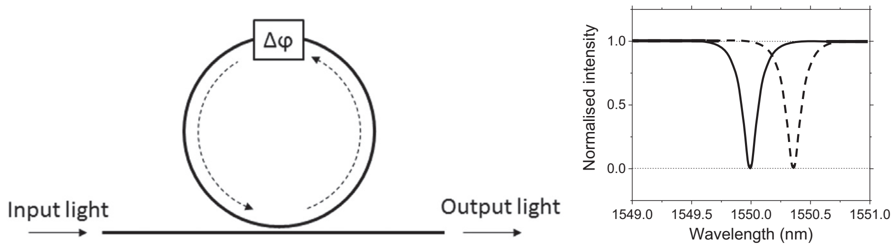

Figure 3.10 Diagram of a ring resonator-based modulator.

the device resonates. When the ring resonator is at resonance, a minimum in transmission results, and away from resonance a maximum occurs. In this way, by inputting light into the device which is initially at resonance and then using the phase modulator to shift the resonant wavelength of the ring away from that of the input light, the transmission can be moved from a minimum to a maximum.

The transfer function of the ring resonator with two different drive conditions is shown in Fig. 3.10. We show the case where the resonance depth is large, which occurs at critical coupling, where the ring round-trip losses are such that the intensity in the ring at the coupling point equals the light coupled into the ring. If these intensities are not balanced, the ring may be under or overcoupled and the depth of the resonance reduced. The quality factor (Q) of the ring is a very important parameter which is dependent on the round-trip losses. A large Q will provide a narrow resonance meaning that only a small shift in the resonance wavelength is required to achieve a large degree of IM. A large Q, however, implies that the photon cavity lifetime will be large restricting the speed of modulation. Therefore a compromise of the Q is required to have both efficient modulation and high-speed operation.

3.4.1.3 Interferometric versus resonant approaches

Table. 3.1 summarizes the comparisons between MZI and ring modulators. In comparison with MZI modulators, the ring modulators benefit from compact size, resulting in a lower capacitance that can be driven as a lumped element with higher bandwidth, lower power consumption around 10 seconds of fJ/bit. However, resonant devices are wavelength dependent, more sensitive to both fabrication errors and temperature changes implying that more active tuning would be required to hold the device at the correct operating point. The power required for the control circuitry and tuning mechanism used to stabilize will therefore likely be much larger. The overall power consumption will depend strongly on how the device is to be operated and the environment in which it is required to operate.

3.4.2 Examples of interferometric and resonant devices employing the Free-carrier plasma dispersion effect

In this section, examples of interferometric and resonant devices based on carrier injection, depletion, and carrier accumulation are presented.

Table 3.1 State of the art of different types of silicon modulators.

	Mach–Zehnder interferometer modulators	Resonant photonic modulators
Compactness	> 1 mm	<20 μm*2π
Wavelength dependence	Broadband	*Discrete resonances, <0.5 nm*
Temperature sensitivity	Less sensitive	Highly sensitive
Insertion loss	High	*Low*
Sensitivity to fabrication error	Less sensitive	Higher sensitivity
Power consumption	>1 pJ/bit	*10 s fJ/bit*
Capacitance	High	*Low*
Bandwidth	Low	*High*

The overall performance of a given device should be assessed taking into account the different performance metrics, efficiency, IL, operating speed, optical bandwidth, etc. Many of these metrics can be traded off against one another. For example, increasing the carrier doping levels generally increases the operating speed, but also increases optical loss. A figure of merit taking into account all of the considered performance metrics can be used to give an overall picture; however, this may not necessarily give an indication of the best device for a given application. Therefore we summarize the current state of the art in Table 3.2, for some of the critical performance metrics to give an idea of the bounds of performance achievable.

The state of the art of carrier injection modulators allows data rates up to 90 GBaud but with external circuits for equalization to extend the bandwidth, indicating that the device performance is not comparable with carrier depletion modulators in terms of efficiency and bandwidth, as summarized in Table 3.2. The carrier depletion and carrier accumulation approaches have been widely studied as they are the practical options for high-speed data modulation without any (or with less complicated) preemphasis drive techniques. The carrier accumulation modulators were first reported with 1 Gb/s data rate in 2004 and have experienced a large improvement to reach 40 Gb/s in 2014 by using horizontal MOS junctions with CMOS drivers and 60 Gb/s by using vertical MOS junctions by external driver probing method. The experimentally demonstrated vertical MOS junction modulators are compatible with popular thin SOI photonics platforms (with mature silicon depletion modulators) and show promise to reach high-speed, compact, lumped MZI modulators in comparison with depletion MZI modulators typically with traveling wave electrodes. Silicon depletion modulators are the most widely studied devices that have been optimized with data rates beyond 100 GBaud [56] and co-integrated with CMOS drivers [45].

3.4.3 Electro-absorption modulators

The major EA modulation mechanisms such as the FKE in bulk material and QCSE in QW layers have been demonstrated in bulk germanium and GeSi alloys. EA

Table 3.2 State of the art of different types silicon modulators.

References	Year	Optical structure	Doping structure	Efficiency (V · cm)	Insertion loss (dB)	ER (dB)	V_{pp} (V)	Bitrate (Gb/s)	Size
Carrier injection									
Xu et al. [10][a]	2007	Ring	PIN	–		9	8	12.5	5 μm *2π
Meister et al. [47]	2013	Nano cavity	PIN	0.014	6	10	2.7	12.5	8.8 μm
Akiyama et al. [48][a]	2013	MZI	PIN	0.01	7.2	4.3	4.35	50	250 μm
Shakoor et al. [49]	2014	Nano cavity	PIN	–	1	8	0.5	3	3.5 μm
Sobu et al. [50][a]	2021	MZI	PIN	2	2.78	3.1–1	7.2–2	50–90	1000 μm
Carrier accumulation									
Liu et al. [36]	2004	MZI	Horizontal MOS	8	6.7	16	7.7	1	2.5 mm
Van Campenhout et al. [51]	2012	Ring	Horizontal MOS	0.24	3	8	1.5	3	2.5 μm *2π
Webster et al. [52]	2014	MZI	Horizontal MOS	0.2	–	8	1	40	400 μm
Sodagar et al. [53]	2014	Microdisk	Horizontal MOS	–	5	8	4	15	3 μm *2π
Debnath et al. [54]	2018	MZI	Vertical MOS	1.53	2.5	3.65	6	25	500 μm
Zhang et al. [55]	2021	MZI	Vertical MOS	1.8	–	–	4	60	200 μm
Carrier depletion									
Liao et al. [42]	2007	MZI	Horizontal PN	4	4	1.1	6	40	–
Thomson et al. [44]	2012	MZI	Vertical PN	2.8	3.7	5.5	6.5	50	1 mm
Li et al. [45][b]	2020	MZI	Vertical PN	1.5	6.9	3	~3	>100	2.47 mm
Sakib et al. [56]	2021	Ring	L-shape PN	0.53	9	3.9	0.8	128	6 μm *2π

MZI, Mach–Zehnder interferometer.
[a]Electrical driving signals are with preemphasis.
[b]CMOS driver codesigned for high bandwidth silicon modulator.

modulation is obtained for a narrow wavelength range by varying the imaginary part of the refractive index with an electric field as theorized independently by Franz [57] and Keldysh [58] and, therefore, the absorption coefficient of the material becomes proportional to the electric field strength. Thanks to the germanium direct bandgap around 0.8 eV (corresponding to 1550 nm), FK-based transceivers operating in the C-band telecommunication window can be integrated to a silicon photonic platform. GeSi with a low Si content ($\sim$1.5% [14]) is often used to tailor the operation point by varying the direct bandgap energy and/or by engineering the strain accumulated, when the alloy is grown [59]. More recently, the engineering of epitaxial growth techniques allowed deposition of QWs to exploit the QCSE in waveguides utilizing Ge, GeSi [16,60–65]. QWs allow for a wider wavelength range of operation, a graphical comparison of the energy bandgap for bulk material and QW is depicted in Fig. 3.11. In a bulk material the energy bandgap can only be varied by changing the material composition and/or applying strain. In a QW the electronic behavior can be tailored and the nanostructure thickness affects the bandgap energy as illustrated in Fig. 3.11 (arrows from orange to blue).

The benefit of using QCSE-type devices becomes clear as deposition engineering allows shifting of the operation band of such a modulator from the O-band to the C-band by modifying strain and quantum confinement [67].

The integration of EAMs into a CMOS photonic platform is enabled through the formation of a PIN diode (Fig. 3.12) integrated into a portion (<100 μm) of the waveguide. The diode is driven in reverse bias as a lumped element circuit. When no bias is applied, the propagating optical wave is partially absorbed due to the built-in electric field, whereas at reverse bias the absorption increases, where the

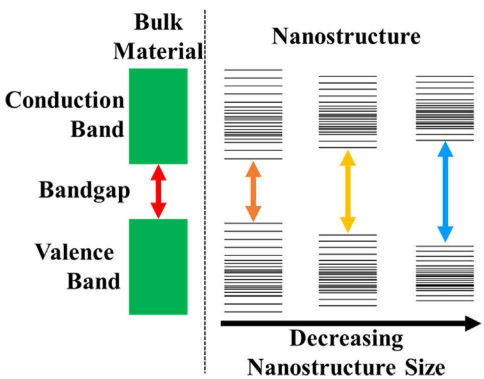

Figure 3.11 Comparison of the bandgap energy for bulk and QW semiconductors. In bulk the bandgap is fixed and depends on the material composition, it can be varied with external forces such as strain. In QWs the quantum confinement increases the bandgap if the size of the nanostructure reduces [66]. *QW*, Quantum well.
Source: Reproduced from L. Mastronardi, GeSi Franz-Keldysh modulator for silicon photonic integrated circuits (Doctoral thesis), University of Southampton, 2019. <https://scholar.google.co.uk/scholar?hl = en&as_sdt = 0%2C5&q = GeSi + Franz-Keldysh + modulator + for + silicon + photonic + integrated + circuits&btnG = > (accessed 09.10.21).

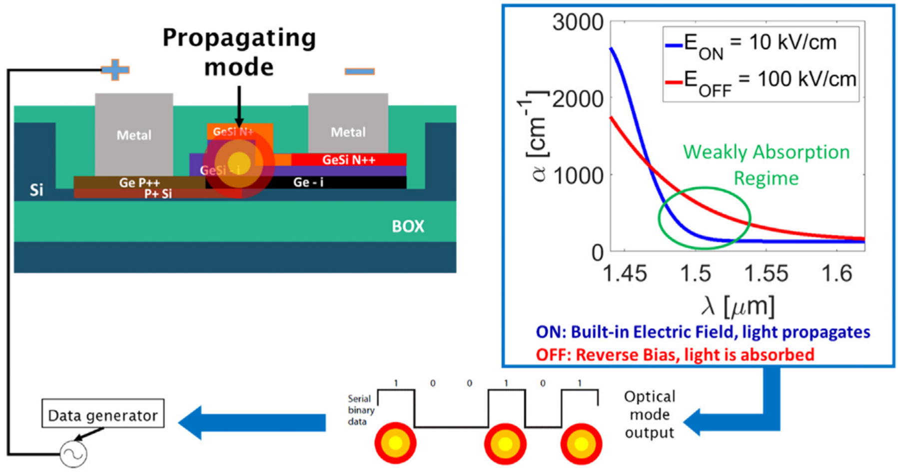

Figure 3.12 PIN FKE modulator cross section and absorption coefficient versus wavelength with (red) and without (green) reverse bias. The PIN diode is integrated to a waveguide, where the mode propagates through the intrinsic region of the PIN junction. *FKE*, Franz–Keldysh effect.

difference in absorption is proportional to the strength of the electric field and length of the modulator.

Typically, EAM FKE-based devices have a relatively small footprint in the region of 60 μm^2, resulting in a low power consumption (<50 fJ/bit) and display data rates in excess of 50 Gbps with the possibility to operate in TE and TM polarizations. The operational bandwidth is typically in the order of 30 nm within the C-band. QCSE modulators [60] are also implemented using PIN diodes, where the stronger field effect and the extended operation regime are counterbalanced by a more complex integration process compared to FKE modulators.

The difficulties of integration of QCSE structures are linked to the mode matching and interfacing of a relatively large QCSE QW stack waveguides to a smaller silicon waveguide. A recent demonstration of integration of QSCE QW in silicon waveguides is illustrated in Fig. 3.13.

Table 3.3, summarizes a range of integrated EAMs using Ge [68,69] and operating in the L-band as well as EAMs using GeSi [14,70,71] with varying operational points in the C-band. Demonstrated EAMs have reached data rates beyond 56 Gb/s with low power consumption (12.8 fJ/s), low dark current (< 47 nA), and compact design (down to 16 μm^2 [68]). The optical bandwidth ranges between 14 [18] and 35 nm [68,69,71]. Coarse wavelength division multiplexing (CWDM) [72] increases the optical bandwidth up to 80 nm at the cost of speed, limiting the speed in this example to 10 Gb/s, and power consumption (5.82 mW per channel).

In Table 3.4, QCSE-based devices are summarized that have been demonstrated to operate in the E-band [16,61] or C-band [62,63] with low power consumption (8.25 fJ/bit [63]) and compact footprint (120 μm^2 [7]). Recently, waveguide-integrated

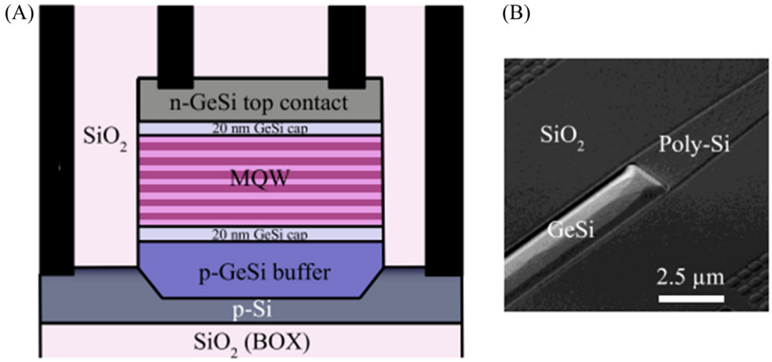

Figure 3.13 (A) Cross section of the QCSE EAM. (B) SEM image of the waveguide QCSE EAM coupled to a poly-Si waveguide. *EAMs*, Electro-absorption modulators; *QCSE*, Quantum-confined stark effect; *SEM*, Scanning electron microscope.
Source: Reproduced from C. Porret et al., "O-band GeSi quantum-confined stark effect electro-absorption modulator integrated in a 220nm silicon photonics platform," in: *2020 IEEE Symposium on VLSI Technology*, 2020, pp. 1–2, https://doi.org/10.1109/VLSITechnology18217.2020.9265082.

QCSE EAMs operating in the O-band [60] and C-band [64,65] have been proposed, showing wide optical operation range, low power consumption, compact design, and a relatively large ER.

3.4.4 Modulator driver amplifiers

In the optical transceiver link, a modulator driver operates as a broadband amplifier and sees the optical modulator as a low-impedance load. The driver amplifier accepts a low-voltage swing signal from the preceding stage, such as a multiplexer or predriver, and amplifies the signal up to several volts. There are many metrics when evaluating the performance of a driver amplifier, and the most common specifications are bandwidth and group delay, voltage swing, and power efficiency.

3.4.4.1 Bandwidth and group delay

The bandwidth of the typical broadband driver can be defined as the 3-dB bandwidth of the voltage gain (S21 in dB). Meanwhile, the group delay, which is a measure of phase distortion over the frequency range of interest, plays a dominant role when the bandwidth of the amplifier extends into the millimeter wave range. Most driver amplifiers need to cope with broadband signals ranging from several kHz to tens of GHz. Owing to the adoption of on-chip peaking inductors/transformers, it is possible to broaden the gain-bandwidth product of the amplifier. However, it is much more challenging to maintain a constant group delay over the entire frequency range, especially when the modulator is integrated. An example of this

Table 3.3 Recent progress in silicon Franz–Keldysh modulator.

References	λ (nm)	Area (μm^2)	3db band (GHz)	Speed (Gb/s)	ER dynamic (dB)	Voltage (V)	Dark current (nA)	Energy (fJ/bit)	IL (dB)	ER (dB)
Liu et al. [70]	1550	0.6×50	1.2	–	–	3 (V_{pp}) -4 (bias)	< 65	50	7.5	10
Feng et al. [71]	1550	0.8×50	38	28	4.5	3 (V_{pp}) -3 (bias)	15.4×10^3	147	4.8	5.9
Lim et al. [68]	1600	16	–	1.25	–	-5 (bias)	–	–	9.6	10
Srinivasan et al. [69]	1610	0.6×40	>50	56	3.29	2 (V_{pp}) -2 (bias)	<47	12.8	4.9	4.6
Mastronardi et al. [14]	1566	1.5×40	56	56.2	5.2	4 (V_{pp}) -2.7 (bias)	2×10^3	44	10.6	5.7

ER, Extinction ratio.

Table 3.4 Recent progress in silicon Quantum-confined stark effect modulator.

References	λ (nm)	Area (μm²)	3db band (GHz)	Speed (Gb/s)	ER dynamic (dB)	Voltage (V)	Energy (fJ/bit)	IL (dB)	ER (dB)
Rouifed et al. [16]	1400	3 × 50	–	–	–	4 (V_{pp}) − 4 (bias)	22	3	4
Chaisakul et al. [61]	1433 1444	3 × 90	23	–	–	1 (V_{pp}) − 3, −4 (bias)	108	5.5 12	10
Edwards et al. [62]	1550 1490	0.6 × 200	–	–	–	1 (V_{pp})	–	3.5−4.5 6.5−8	6.5 15
Roth et al. [63]	1541	225 × 625	–	–	–	1 (V_{pp}) − 1 (bias)	8.25	–	3
Ren et al. [64]	1425 1548	8	–	7 @ 1460 nm (oscilloscope trace)	3.2 @ 1460 nm (oscilloscope trace)	1 (V_{pp}) − 6.5 (bias)	–	–	2.84 (photocurrent)
Zang et al. [65]	1450 1550	100 × 2	–	–	–	1 (V_{pp}) − 1, −3 (bias)	–	–	~1.4 (photocurrent)
Porret et al. [60]	1350	~2 × 40	–	–	–	1 (V_{pp}) − 1 (bias)	–	16	8

ER, Extinction ratio.

dilemma is demonstrated in Ref. [73] where an outstanding bandwidth from DC to 108 GHz had been delivered, whereas its group delay variation is up to 80 ps over that frequency range. Therefore we have seen that most commercial driver amplifiers can only deliver a usable bandwidth up to 70 GHz, which is approximately equal to a symbol rate at 100−120 GBaud.

3.4.4.2 Voltage swing and power efficiency

The voltage swing of a driver is normally expressed as "V_{pp}" for a single-ended output voltage swing or "V_{ppd}" for differential outputs. Traditionally, these figures are measured by feeding the output node of the driver into a digital oscilloscope, which is assumed to be exactly 50 Ω. Commonly, a driver should provide a single-ended output swing up to several volts [74−76]. The power consumption (in mW) divided by the operation speed (Gb/s) generates a figure for power efficiency (mW/Gb = pJ/bit). Obviously, a higher voltage swing drives more current and hence comes with an inferior power efficiency (energy/bit). This figure of merit is typically used to evaluate the performance of a driver. However, these figures become meaningless when the driver is custom designed for a bespoke modulator. For example, the drivers in Ref. [77] designed for ring resonators see the load as a lumped capacitor, whereas some drivers are designed for traveling wave modulators and see a load significantly less than 50 Ω [78]. Furthermore, the adoption of complex modulation formats makes it even harder to make a fair comparison, as complex modulation formats always come with a lower signal-to-noise ratio. Therefore it has become common to combine the optical ER and power efficiency figure: power efficiency = power/(data rate*ER) [79]. This figure provides a relatively fair comparison of different types of modulator and different modulation schemes.

3.4.4.3 Circuit topology

When it comes to practical implementation, the circuit topologies of the driver amplifier could be classified into two categories: voltage [80−83] and current modes [75,76]. In both approaches, stacked transistors are adopted to protect the switching transistors from voltage breakdown issues and to withstand the high voltage swing.

Fig. 3.14A shows that the voltage-mode approach takes advantage of the CMOS process by configuring the PMOS and NMOS transistors as push−pull amplifiers. During the operation, either the PMOS or NMOS is switched on at any one time hence eliminating static current flow. Therefore this configuration is preferred due to its potential for lower power consumption. However, the switching behavior of PMOS and NMOS leads to a dynamic change of the output impedance when transistors operate in different operating regions. Even with a built-in impedance control module [81], it is hard to maintain a constant output impedance over a broadband frequency range. As a result, the voltage-mode approach is usually utilized to drive lumped elements, such as ring resonators [80,82] or small segments within a Mach−Zehnder modulator (MZM) [79,84]. Furthermore, another unavoidable issue

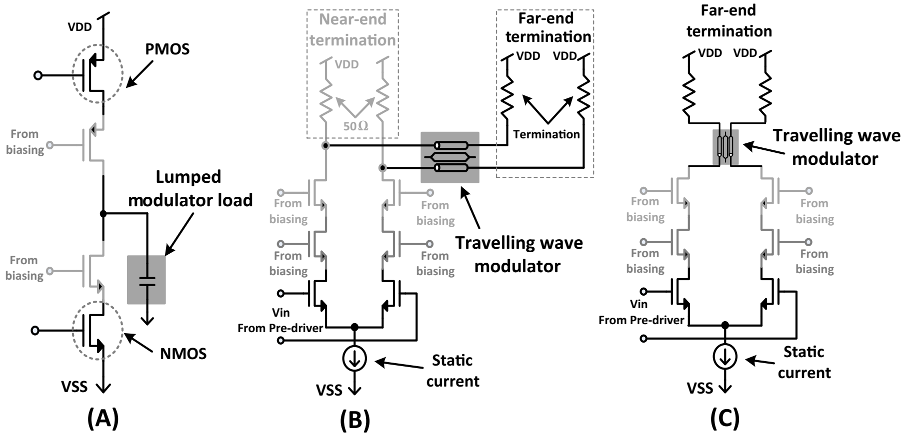

Figure 3.14 (A) Voltage-mode push−pull driver integrated with lumped element. (B) Current-mode driver amplifier with double termination. (C) Open-drain driver amplifier integrated with traveling wave modulator.

is the relatively low transition frequency (*ft*) of the PMOS transistor, which becomes a major bottleneck for higher speed applications. The highest baud rate of reported voltage mode drivers can be found in Ref. [83], which is realized on the 28 nm FD-SOI process and operates up to 60 GBaud [on−off keying (OOK)].

In contrast to the push−pull amplifier, as shown in Fig. 3.14B, the current-mode approach eliminates the PMOS transistors and hence avoids the speed limitation issue. By switching the NMOS transistors within a CMOS process or NPN bipolar transistor in a BiCMOS process, the current is switched between two pairs of termination resistors (near-end 50-Ω resistors and far-end termination resistors) and hence a reliable impedance matching over the broadband frequency range is provided. Therefore current mode has become the primary choice for modulators that are built in a traveling wave configuration (such as the MZM). The major concern with the current mode approach is the relatively low power efficiency, which comes as a result of needing to deliver current flow to four parallel load resistors.

Therefore, as shown in Fig. 3.14C, a popular solution is to eliminate the two near-end termination resistors and hence significantly reduce the power consumption. This kind of configuration is called an "open-drain amplifier" and has been adopted in many recent demonstrations [78,85,86]. However, the precondition is the precise control over device packaging so that the parasitic effects (from wire bonding and/or flip-chip bonding) that induce impedance discontinuities are minimized. Even if the impedance discontinuity issue can be alleviated, a major concern is that the system bandwidth is predominantly determined by the bandwidth of the electrodes of the traveling wave modulator. An example is reported in [78], in which two segments of traveling wave modulator are monolithically integrated with two separate open-drain amplifiers. The length of the first segment is twice that of the second, and the first segment E-O bandwidth is significantly lower (by more than 50%) than the second one.

3.4.4.4 Codesign of driver and modulator

To tackle the demanding technical challenges in the field, the modulator and driver amplifier must be considered a single integrated system. This means that neither the amplifier nor the optical modulator can be treated as a standalone component, and the realization of system functionality depends on the integration of these functions at the design stage. Next, we highlight the three most common schemes that have been developed in the field.

1. Segmented modulator integrated with driver amplifier

   Segmented modulators, codesigned and copackaged with a number of driver amplifiers, offer a variety of advantages for high-performance transmitters, where advanced modulation formats [22,36–40] (such as PAM-N and QAM-N), high ER [79,87], or optical signal shaping (such as optical feed-forward equalization) [88] have become the system requirement. As shown in Fig. 3.15A, the phase shifter is divided into a number of segments, with each segment fed with an independent electrical signal. With such a configuration, each driver unit only sees a small portion of the phase shifter, which is seen as a lumped element to the driver amplifier, and hence the power-hungry termination resistors can be eliminated.

   However, a major challenge for this scheme is that the timing of the electrical signals needs to be matched with the propagation delay of the optical signal. As a result, a timing control function (τ) is always built within each electrical driver amplifier. In practical implementations, this time delay function could be realized with a passive device, such as an on-chip transmission line [87], or with active components, such as a tunable delay element [89]. Both schemes introduce additional overhead (power and chip area) to the system and suffer from the unavoidable process–voltage–temperature variations.

2. Inductive peaking

   Inductive peaking is a standard technique that has been utilized for bandwidth enhancement in numerous high-speed electrical circuit designs. When a driver amplifier sees a photonic device configured as a lumped element, the device capacitance creates a low

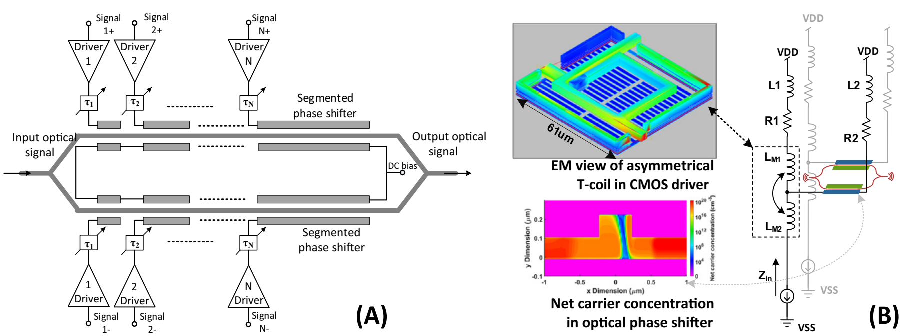

Figure 3.15 (A) Conceptual model of segmented modulator integrated with driver amplifier. (B) T-coil peaking embedded in between the driver and traveling wave modulator.

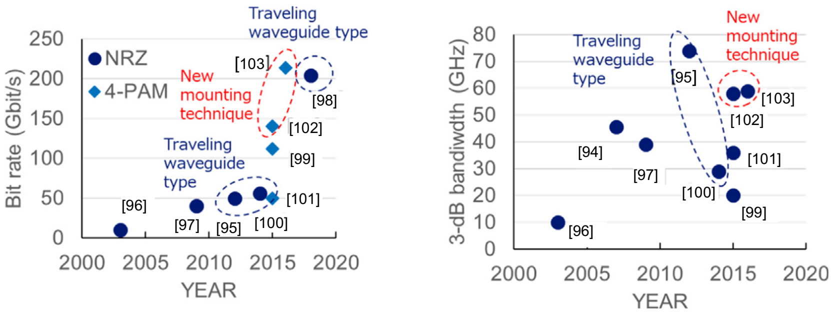

Figure 3.16 Bitrate and 3-dB bandwidth change of EA modulators [91–100]. *EA*, Electro-absorption.

impedance load at high frequency. When a driver amplifier is integrated with a traveling wave modulator, the radio frequency (RF) loss of electrodes could significantly degrade the system bandwidth. In either case, a precisely modeled peaking inductor between the photonics and electronic devices can dramatically boost the system bandwidth. This inductor could be realized with a bonding wire [80] or with T-coil peaking [45,90]. As shown in Fig. 3.16B, an on-chip asymmetrical T-coil is embedded between the driver amplifier and the traveling wave modulator. According to Ref. [45], such a configuration can offer an additional 70% bandwidth enhancement over traditional peaking inductors and also demonstrates that copackaged driver and modulator could operate up to 112 GBaud. The concerns with this technique are the additional chip area on the driver chip and the variation of group delay at high frequencies.

3. Nonlinearity cancellation

Due to the raised cosine transfer function of the MZI, nonlinearity issues always exist when complex modulation formats (PAM-N/QAM-N) are utilized. To address this concern, the segmented MZI design [101] has introduced additional segments and has been integrated with a corresponding driver to compensate the nonlinearity. In Ref. [81] a driver that is integrated with a traveling wave modulator has incorporated an additional predistortion function to compensate the nonlinearity. The nonlinearity issue also exists within ring resonator modulators. The Lorentzian shape of E-O transfer characteristics leads to a wavelength-dependent static nonlinearity. Different bias voltages also dynamically change the small signal bandwidth which produces a dynamic nonlinearity. Recent work from Intel [77,80] has introduced nonlinear feed-forward equalization within the driver circuit itself and through this approach, an experimental demonstration of a 112-Gbps PAM-4 signal, with a measured Transmitter Dispersion Eye Closure Quaternary (TDECQ) less than 1 dB has been possible.

3.5 III–V modulators

In this section, we describe III–V compound semiconductors modulators for high-speed optical communication systems. A directly modulated laser (DML) is the simplest method of generating the signals by changing the injection current, providing a low-cost and low-power solution. However, there are limitations such as modulation speed and frequency chirp (i.e., transmission distance). EA and MZM III−V modulators require separate light sources but overcome these drawbacks. Table 3.5 compares vertical-cavity surface-emitting lasers (VCSELs), distributed feedback (DFB) lasers, EA modulators, and MZMs. Directly modulated multimode VCSELs are typically limited to less than 50 Gbit/s and the transmission distance is limited to ~100 m. DFB lasers provide greater power and extend the transmission range, although they are limited by frequency chirp when directly modulated. III−V modulators use an MQW, where the detuning between the operating wavelength and the exciton peak wavelength is ~50 nm for the EA modulator and ~150 nm for the MZM modulator. The EA modulator with a several-hundred-μm length is suitable for IM with a bitrate of over 50 Gbit/s by using the QCSE. As the detuning increases, it can be used as a phase modulator with small IM. Thus III−V MZMs are suitable for generating signals with advanced modulation formats such as quadrature amplitude modulation (QAM) that can increase throughput and transmission distance. However, because the modulation efficiency is low and the length of the phase modulator requires several mm, its large footprint is costly.

3.5.1 Conventional III−V modulators

EA modulators and MZMs have been used in relatively long transmission distance and high-capacity networks to overcome the limitations of DMLs. In addition, these devices are suitable for uncooled operation because the modulation speed is independent of the operation temperature. This is important because the removal of the thermoelectric cooler reduces the overall power consumption.

Fig. 3.16 shows the throughput and 3-dB bandwidth progression of EA modulators. Because the detuning of MQW is set small for IM, the EA modulator enables us to achieve large ER with several-hundred-μm active length. A 3-dB bandwidth of more than 40 GHz is achieved by using the conventional lumped electrode [91]. To further increase the bandwidth, an EA modulator using a traveling wave type of electrode has achieved a 3-dB bandwidth of more than 70 GHz [92]. As Table 3.5 shows, an EA modulator monolithically integrated with DFB lasers (externally modulated lasers (EMLs)) has been reported as a high-speed and small-chip-size optical light source [91,93−97] that can reduce the device cost.

Fig. 3.17 shows the throughput and 3-dB bandwidth change of MZMs. The MZMs generate optical signals by changing the refractive index using the QCSE and the Pockels effect. The length of the phase modulator is several mm because the detuning of the MQW is set to be large enough to avoid large absorption. Therefore the traveling-wave electrode is key to achieving a high modulation speed. For this purpose, there are two designs: a capacitance-loaded traveling-wave electrode (CL-TWE) and an n-i-p-n structure. Due to low resistance, MZMs with n-i-p-n CL-TWE have achieved a 3-dB bandwidth of more than 67 GHz, which is the measurement limit [102,103]. The MZMs can generate phase modulation format optical signals that include quadrature phase-shift keying and 16QAM [103−105].

Table 3.5 Comparison summary of vertical-cavity surface-emitting lasers (VCSELs), distributed feedback lasers, electro-absorption (EA) modulators, and Mach−Zehnder modulators (MZMs).

	VCSELs	**Directly modulated laser s**	**EA modulators**	**MZMs**
Schematic structure	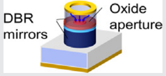	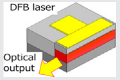	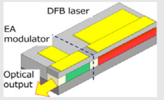	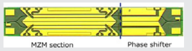
Power consumption	Very low	Very low	Low	Little high
Optical output power	Very high	Very high	High	Little low
Chip size	Very small (0.1−0.3 mm × 0.1−0.3 mm)	Very small (0.2−0.4 mm × 0.15−0.2 mm)	Small (0.2−0.4 mm × 0.5−1.0 mm)	Large (0.5−2.5 mm × 3.0−7.0 mm)
3-dB bandwidth	~30 GHz	<40 GHz	~100 GHz (traveling wave type)	>67 GHz
ER	<6 dB	<6 dB	~8 dB	~10 dB
Chirp parameter α	~3.0	~3.0	0−10	0

ER, extinction ratio.

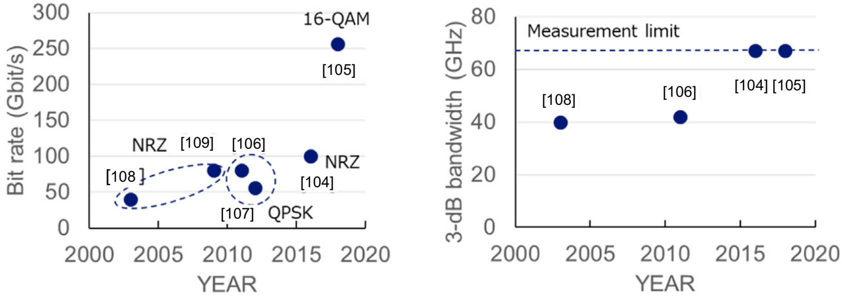

Figure 3.17 Bitrate and 3-dB bandwidth change of MZMs. [102−107]. *MZMs*, Mach−Zehnder modulator.

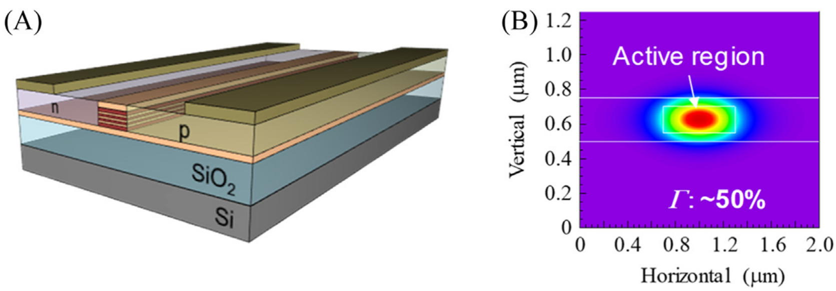

Figure 3.18 (A) Schematic diagram of membrane photonic device. (B) Calculated optical mode profile.

However, the disadvantages are the large chip size and the transmitter loss, which includes MZMs, a polarization convertor, and waveguides.

3.5.2 Membrane III−V modulators

The increase in optical confinement factors has been a focus in studies on achieving high modulation efficiency that results in low power consumption. Fig. 3.18A shows a schematic diagram of membrane III−V devices on SiO_2/Si substrate, in which a ~250-nm thick III−V layer with a lateral *pn* junction is sandwiched between low refractive index materials [108−113].

An optical confinement factor three times that of the conventional III−V modulator could be obtained from this structure, as shown in Fig. 3.18B. Utilizing a buried heterostructure can efficiently confine carriers and photons. Furthermore, integration with the Si waveguide is easy because the membrane III−V device has a size and effective refractive index similar to the Si waveguide. Fig. 3.19A shows a microscope image of a membrane MZM integrated with a membrane DFB laser [114]. The authors connected the laser and the phase modulator with a silicon 2 × 2 multimode interferometer. The active region length was 500 μm for both the laser

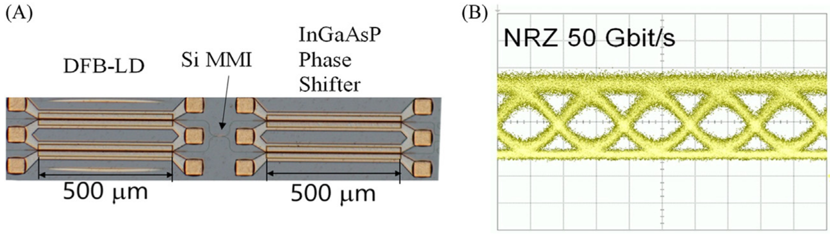

Figure 3.19 (A) Photograph of monolithically integrated MZM and DFB laser. (B) Eye diagram with 50 Gbit/s NRZ signal modulation. *DFB*, Distributed feedback; *MZM*, Mach–Zehnder modulator.

and the phase modulator. An n-doped bulk InGaAsP was used for the phase modulator, and the measured V_π ranged from 7.6 to 8.2 V, which corresponded to the $V_\pi L$ of around 0.4 V · cm. Due to the large optical confinement factor and the small capacitance of the membrane structure, 50-Gbit/s nonreturn-to-zero (NRZ) modulation performance using lumped electrode design was realized, as shown in Fig. 3.19B.

3.6 Heterogeneous integration on silicon

This section discusses recent work on combining a range of materials with the silicon photonics platform to exploit the benefits of heterogeneous integration. Each of the material integration strategies is discussed in turn.

3.6.1 III–V on silicon

As discussed earlier, the key metrics for a modulator are small size, low loss, low drive voltage, and high bandwidth. The first three metrics all improve with a larger modulation efficiency, and the last metric also depends on modulation efficiency because smaller devices have less microwave loss, resulting in larger bandwidths. Si modulators use the plasma effect to change the index and that works well and is widely used. III–V materials have a plasma effect, but also band filling, Kerr and Pockels effects, as shown in Fig. 3.20, their modulation efficiency tends to be about 10 times larger [115,116]. The plasma effect is orientation independent, but the Pockels effect is orientation dependent, so modulators must be properly oriented for the best performance. MZI modulators using III–V on Si have been demonstrated with bandwidths of 25 GHz and $V_\pi L$ of 2.4 V_{mm} [115]. Smaller, higher speed devices can be fabricated using EA [92]. Low power can be achieved with short devices operating at high impedance, but larger bandwidths typically require traveling wave designs with 50-Ω impedance as shown in Fig. 3.21, and bandwidths in excess of 67 GHz with modulation efficiency of 4.3 dB/V have been demonstrated [92].

The lowest power Si modulators utilize the MOSCAP design described earlier [36], but bonded III–V on Si MOS modulators have even lower drive voltages due

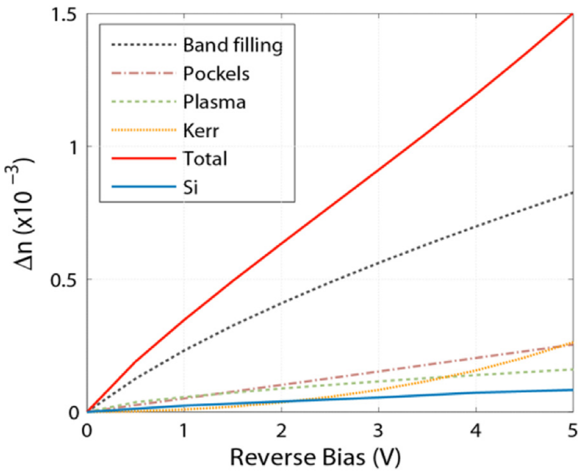

Figure 3.20 Index change per volt of Si (blue) and III−V (red) materials showing the relative contributions of bandfilling, plasma, Kerr, and Pockels effects for InGaAsP. *Source*: After H.-W. Chen, "High-Speed Hybrid Silicon Mach-Zehnder Modulator and Tunable Microwave Filter," University of California, Santa Barbara, 2011.

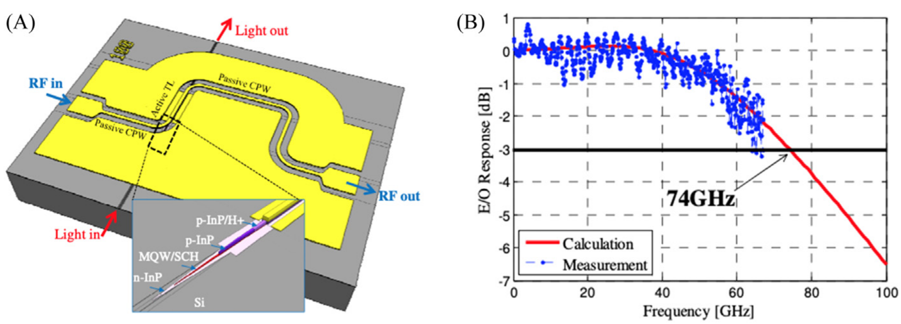

Figure 3.21 (A) Schematic diagram of an HSEAM. (B) Frequency response of the HSEAM modulator. *HSEAM*, Heterogeneous silicon electro-absorption modulator.

to the larger modulation efficiency of III−V materials. A schematic diagram of the ring version of this modulator is shown in Fig. 3.22 along with a transmission electron microscopy (TEM) cross-sectional image of the MOS capacitor. When this capacitor is charged or discharged by applying an electrical field between the III−V material and Si, the carrier concentration around the gate oxide can change by several orders of magnitude to exceed $10^{20}/cm^2$. Because this capacitor (dis) charge process occurs under a fast electric field effect, 40 Gb/s NRZ modulation is possible. However, compared with the pure Si design where deposited poly-Si is typically used as the top layer above the gate oxide, a wafer-bonded III−V layer offers three advantages with respect to its material characteristics: first, crystalline

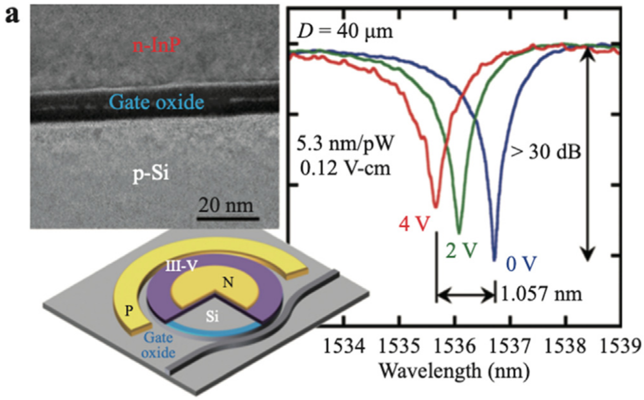

Figure 3.22 Schematic device structure and a cross-sectional TEM image of a III−V/SiO_2/Si MOS modulator. Also shown is the modulator loss for several voltages [119].
Source: After T. Hiraki et al., Heterogeneously integrated III-V/Si MOS capacitor Mach-Zehnder modulator, Nat. Photonics, 11 (8) (2017) 482−485.

III−V material has lower optical loss than poly-Si, even though it is highly doped. Second, the much smaller effective mass and larger mobility of electrons in a III−V material result in a larger real part change in the modal index, which translates into larger phase change efficiency and lower free-carrier absorption. Finally, the band-filling effect in a III−V material contributes to the phase change in addition to the plasma dispersion effect (Fig. 3.20). The $V_\pi L$ of a high-speed modulator is just 0.12 V · cm with a record tuning energy efficiency of 5.3 nm/pW. This is a huge improvement over conventional thermal and carrier injection tuning with a few or sub-nm/mW efficiency. An interesting configuration is to integrate this ring modulator with a gain region, resulting in a three-terminal configuration [117] with potentially all of the advantages of loss-modulated lasers rather than current-modulated lasers [118].

3.6.2 Organic electro-optic materials on Si

Integration of organic materials on silicon waveguides allows a combination of the tremendous processing advantages of silicon photonics with the wealth of optical properties that can be obtained by molecular engineering of organic materials [120]. Silicon-organic hybrid (SOH) devices have been demonstrated to provide second-order [121,122] and third-order [123] optical nonlinearities as well as optical gain [124,125]. For efficient devices, it is imperative to maximize the interaction of the optical waveguide mode with the organic cladding materials, for example, by exploiting discontinuous field enhancement in slot-waveguide structures [126,127].

The concept of a SOH MZM is sketched in Fig. 3.23A and B. Each arm of the modulator consists of a silicon photonic slot waveguide, comprising a pair of silicon rails. The rails are separated by a narrow slot with typical widths between 80 and

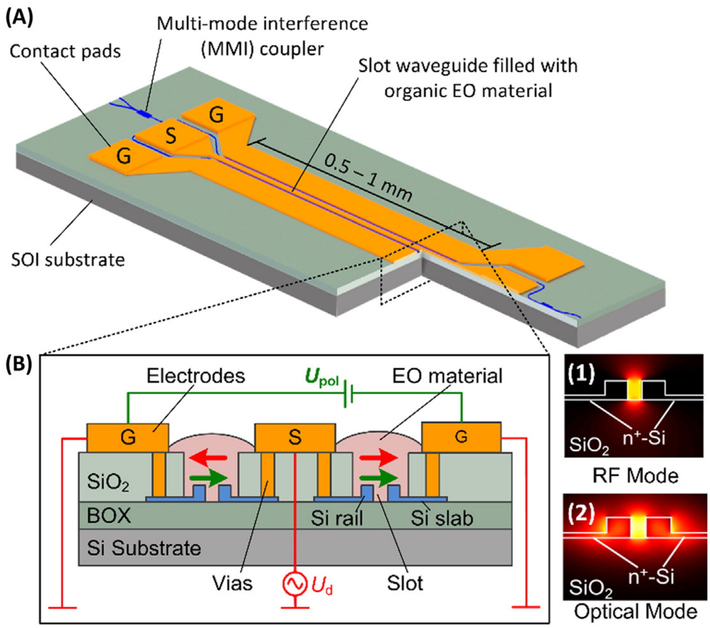

Figure 3.23 Device concept of a SOH EO MZM. (A) Layout of the SOH MZM: silicon photonic slot waveguides are embedded into an organic EO cladding. Light is split by an MMI coupler into the arms of the MZM. (B) Cross section of the SOH MZM: each slot waveguide consists of a pair of silicon photonic rails (width 200−240 nm, height ~220 nm), separated by a slot (80−160 nm). The EO cladding homogeneously fills the slot. The signal is applied via a GSG coplanar transmission line, connected to the rails of the slot waveguide by conductive n-doped silicon slabs (height ~70 nm) and metal vias. For poling of the EO materials, a DC voltage U_{pol} (*green circuit*) is applied across the floating ground electrodes at an elevated temperature. The molecules align accordingly and maintain their orientation (*green arrows*) after cooling. A modulating voltage U_d induces an electric field in the slot (*red arrows*) that is antiparallel in the left to the poling direction, and parallel to the poling direction in the right arm of the MZM, leading to push−pull operation. **(1)** Field distribution of the modulating electrical RF mode. **(2)** Field distribution of the optical quasi-TE mode. The strong overlap of the RF mode and the optical mode leads to highly efficient modulation [128]. *EO*, Electro-optic; *GSG*, ground-signal-ground; *MMI*, multimode interference; *MZM*, Mach−Zehnder modulator; *SOH*, silicon-organic hybrid.
Source: Adapted from O. Marshall, M. Hsu, Z. Wang, B. Kunert, C. Koos, D. Van Thourhout, Heterogeneous integration on silicon photonics, Proc. IEEE, 106 (12) (2018) 2258−2269.

160 nm, and the electrical RF drive signal is applied via a ground-signal-ground transmission line and copropagates with the optical signal along the device. The transmission line is connected to the silicon rails of the slot waveguide by metal vias and thin *n*-doped silicon slabs. The electrical RF voltage drops mainly across the narrow slot, to which the light is strongly confined, thus leading to a strong overlap of the optical mode and the modulating RF field, (see Insets (1) and (2) of

Fig. 3.23B). The $\chi^{(2)}$-nonlinearity of the organic EO material is activated in a one-time poling process by heating the device and by applying an external DC voltage U_{pol} to the floating ground electrodes, thereby aligning the EO molecules as indicated by the green arrows in Fig. 3.23B. The modulating fields (*red arrows*) associated with the RF drive voltage U_d are oriented parallel to the chromophore alignment in one arm and antiparallel in the other arm of the MZM, thereby leading to efficient chirp-free push−pull modulation.

The performance of SOH EO modulators has been demonstrated in a series of experiments, exhibiting remarkable efficiencies with voltage-length products down to $V_\pi L = 0.3$ Vmm and energy consumptions of only a few fJ/bit [129−132]. The viability of SOH devices has been shown both for data transmission using IM and direct detection (IM/DD) [133−135] and for coherent communications [131,132,136,137]. Regarding IM/DD transmission, generation of 100 Gbit/s OOK data signals [134] and 200 Gbit/s PAM-4 was shown [135]. For coherent communications, generation of advanced modulation formats such as 16QAM was demonstrated at ultralow energy consumption [131,132] and with symbol rates of up to 100 GBd transmitted on a single polarization [137]. The extraordinarily low drive voltage of SOH modulators allows operation of the devices directly from standard output ports of field-programable gate arrays without additional drive amplifiers [132]. Besides optical communications, SOH EO modulators have been used for frequency comb generation [138] or as ultracompact phase shifters for optical metrology [139]. SOH devices can be monolithically cointegrated with the full device portfolio of silicon photonics [132], thus offering a route toward highly functional silicon photonic circuits with advanced EO modulators.

The response of the EO cladding materials is ultrafast such that the bandwidth of SOH devices is typically limited by resistive-capacitive (RC) time constants that are associated with the slot capacitance and the resistivity of the silicon slabs [140]. The modulation speed can be greatly increased by plasmonic devices, which reach modulation bandwidths of hundreds of gigahertz [141,142], but suffer from high optical losses, quantified by π-voltage-loss products that are of the order of 10 V dB [122]. This trade-off can be overcome by using optimized doping profiles or [140] capacitive coupling between the RF transmission line and the rails of the optical slot waveguide [143].

Besides boosting the performance of SOH devices, research efforts have also concentrated on improved organic EO materials. In most material systems, less than 15% of the EO activity inherent in the chromophores is translated to macroscopic EO effects by poling. Improved theoretical methods [120] have led to new classes of organic EO materials and allowed systematic improvements of the poling efficiency. This resulted in macroscopic EO coefficients r_{33} in excess of 500 pm/V in thin films [144−148] and of up to 390 pm/V in SOH devices [130]. Theoretical calculations also suggest that new chromophores with significantly improved molecular first-order hyperpolarizability are possible [148], which would enable SOH modulators with π-voltages of less than 100 mV.

In view of industrial applications of SOH devices, systematic investigation and optimization of thermal and photochemical stability of EO cladding materials is of utmost importance. First investigations have demonstrated long-term thermal stability in accordance with Telcordia standards for high-temperature storage [149], while photochemical stability is the subject of ongoing research. A specific advantage of organic EO materials is that a variety of parameters such as EO activity, optical loss, dielectric permittivity, lattice hardness, material compatibility, and material processability can be simultaneously optimized by systematic chemical modification of the material. SOH devices will hence immediately benefit from future advances in design and synthesis of functional organic optical materials.

3.6.3 Graphene on Si

Graphene is a gapless 2D material with broadband electronic and optoelectronic properties [150,151] and with conduction and valence bands in contact in the neutrality (Dirac) point. The Fermi level, which is related to the conductivity and carrier concentration, can be controlled by applying an external electric field. The gapless nature and the electrical control of carrier concentration lead to broadband EA and electro-refraction. When graphene is integrated into waveguides, efficient active photonic devices such as modulators, detectors, switches, and phase shifters can be realized. Graphene can be conveniently integrated on top of passive photonic platforms such as silicon (Si), silicon nitride (SiN), or other dielectric waveguides [152].

Graphene-based modulation exploits charge accumulation in a capacitor structure [153,154]. The first demonstration of an OOK modulation at 10 Gb/s was achieved with a single-layer graphene (SLG) placed on a thin oxide layer on top of a doped Si waveguide [155]. This device was operated at 1550 nm biased at 0.45 eV doping level and with a swing voltage that permitted the modulation of absorption. More recently, the same design was improved to 16 GHz bandwidth [156]. Larger bandwidth has been reported on SiN [157] and Si passive waveguides [158], up to 39 GHz EO bandwidth, 50 Gb/s data rate [159], and 2.2 dB/V modulation efficiency [160]. In all latter cases, the capacitor was made of two graphene layers spaced by a thin dielectric spacer, the so-called double-layer graphene (DLG). The DLG configuration features several advantages: it does not require carrier implantations or Ge epitaxy because modulation is achieved exclusively with graphene, the modulation efficiency is larger than in the SLG case thanks to the two graphene layers rather than one, and the IL is minimized because the waveguide is undoped. A key aspect of graphene modulators is the quality of graphene in terms of carrier mobility or equivalently in terms of carrier scattering time (Fig. 3.24).

High mobility, of the order of 10,000 cm^2/V/s at 0.1 eV doping level (or 2200 cm^2/V/s at 0.4 eV, that is a typical operating value), determines the minimum background loss of the material, that is, it influences fundamental FoM of modulators such as IL and ER [152]. For high doping levels, say above 0.55 eV at 1550 nm, the graphene response is mainly electro-refractive where phase modulation is dominant, and the modulation efficiency compared to typical Si photonics modulators is larger. A value of $V_\pi L = 0.28\ \mathrm{V \cdot cm}$ measured in an SLG case has

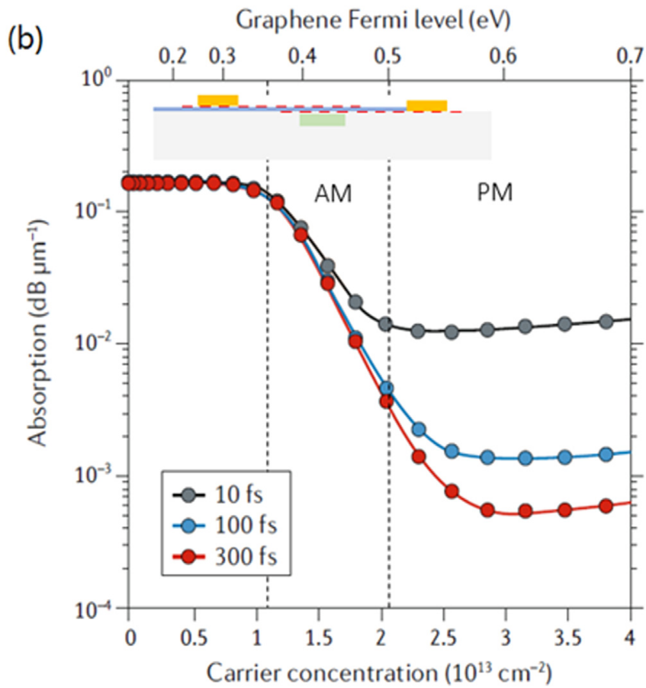

Figure 3.24 Optical absorption at 1550 nm of the DLG on SOI passive waveguide as a function of doping level for three values of scattering time constant (10fs, 100fs, 300fs) showing the effect of the carrier mobility on IL and ER. AM and PM indicate the biasing to operate the DLG in electro-absorption or electro-refraction mode [161]. *AM*, Amplitude modulation; *DLG*, Double-layer graphene; *ER*, extinction ratio; *IL*, insertion loss; *PM*, Phase Modulation; *SOI*, silicon on insulator.
Source: From V. Sorianello, G. Contestabile, M. Romagnoli, Graphene on silicon modulators, J. Light. Technol., 38 (10) (2020) 2782–2789.

been reported [162] whereas a value of $V_\pi L < 0.16\ \mathrm{V \cdot cm}$ for DLG has been predicted [152].

Another key parameter of the graphene modulator is the contact resistance. For high-speed modulators a convenient value is below $250\text{-}\Omega \cdot \mathrm{mm}$, which is a value achievable with both top contact and edge contact technologies [163,164].

Fabrication of graphene modulators requires wafer-scale chemical vapour deposition (CVD) graphene growth and transfer from the catalyst to the photonic wafer. This is mostly a postprocess done in the back end of line. Recently, wafer-scale fabrication has been developed in Si fabs [165] and the process can be compatible with CMOS foundries. This ensures the compatibility of graphene photonics in application-specific roadmaps such as those for optical interconnections and optical communications. Graphene modulators are promising in terms of bandwidth and modulation efficiency. State-of-the-art performances above 100 Gb/s are feasible.

3.6.4 Lithium niobate on Si

LN EO modulators, traditionally realized in bulk LN crystal, have been the workhorse of telecommunication for many decades, owing to their high bandwidth, linear response, and excellent material stability [166]. These legacy devices that rely on low-index contrast waveguides formed by ion indiffusion, or proton-exchange, are usually a few centimeters long and require driving voltage of several volts because of limited EO modulation efficiencies (Fig. 3.25A). The large size, discrete nature, high energy consumption, and high cost make the legacy system unsuitable for modern data communication applications.

Recent development in integrated thin-film LN (TFLN) photonics, enabled by the development of ultralow loss optical waveguides realized using conventional planar fabrication techniques [12], is promising a new class of devices with ultralow driving voltages (<1 V), wide bandwidth (> 100 GHz) and low IL that can be tightly integrated in the same way as silicon photonics devices [167,168]. Achieving a low driving voltage could enable direct CMOS drive that reduces cost, complexity, and energy consumption. Linear and flat response could further reduce digital signal processing workload. The low IL is also key to bringing down total energy consumption in data communication systems. The simple design, proven material property, and excellent thermal stability offer an attractive solution to data communication applications. Recent key demonstrations include 700 Gbps intensity modulated-direct detection (IMDD) using single modulator [169], 1.55 Tbps coherent link at 200 Gbaud [170], and analog modulation up to 500 GHz [171].

The technical breakthrough that enabled these record demonstrations is the ability to fabricate high-confinement and low-loss waveguides in TFLN [172–174]. Achieving low-loss waveguides in TFLN (<0.3 dB/cm) allows the electrodes to be positioned closer to each other than their legacy designs resulting in large $V_\pi \cdot L_\pi$ improvement from about 10 V · cm at 1550 nm [175] in legacy modulators to about 2 V · cm at 1550 nm (1.6 V · cm at 1310 nm) in TFLN [167]. Such a large increase in modulation efficiency results in dramatically improved voltage and bandwidth performance and more dense integration. Two popular modulator integration approaches being explored are (1) directly patterned and etched TFLN-on-insulator

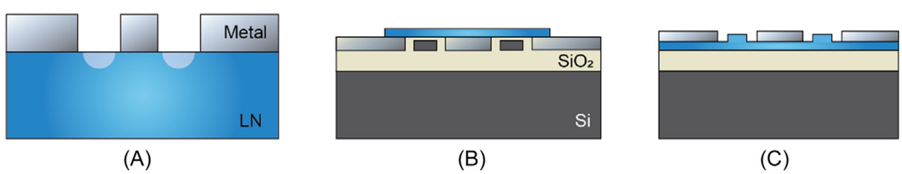

Figure 3.25 Cross section views of lithium niobate electro-optic modulators. (A) Traditional bulk lithium niobate with ion-indiffusion or proton-exchange waveguides, shown in light blue. The electrodes are thick and are separated by large gaps typically more than 10 μm. (B) Thin-film lithium niobate modulator with etched waveguides. The electrode gap can be significantly reduced to 5 μm or less. (C) Thin-film lithium niobate modulator based on back-end processing on a silicon-on-insulator platform. This approach has better compatibility to existing CMOS processes.

to create rib or channel waveguides [17,176] (Fig. 3.25B) and (2) backend film bonding integration allowing the optical mode to be evanescently coupled into a TFLN slab from silicon waveguides (e.g., Refs. [158] [Fig. 3.25C]). While the direct patterning approach has the potential to deliver the best possible modulator performance, the hybrid approach leverages the large library of developed silicon photonics components that can be integrated with TFLN.

The key technical challenge that remains for TFLN is a reliable and cost-effective interface between TFLN modulators, with micron-scale optical waveguides, and single-mode fibers. While the on-chip loss for TFLN modulators has been reduced to sub-dB levels, the fiber interface dominates the optical loss budget. Using concepts similar to those used in silicon photonics mode converters, progress has been made on mode transformation between discrete waveguide layers [177] and integrated edge couplers with lensed fibers, featuring coupling loss <1 dB/facet [178]. The open challenge is to find a high-yield mode converter design and manufacturing process that can be integrated with the silicon platform cost-effectively. This problem is further amplified by a manufacturing challenge: TFLN is not a CMOS-compatible material, and therefore TFLN-integrated photonics will likely require its own dedicated process lines. Early work has demonstrated wafer-scale manufacturability in TFLN-integrated systems, using standard CMOS tools [179] and compatibility with back-end processing in silicon photonics with the film bonding approach [158].

The large boost in performance combined with the ability to integrate modulators with other EO functionalities, such as frequency comb sources [180], on the same TFLN chip, could lead to system-level advantages, thus providing enough incentive to overcome the manufacturing-related capital expenditure. Fundamentally, the TFLN approach can be cost-effective because LN crystals, silicon wafers, and the bonding processes are all low cost and well established. We could envisage TFLN becoming an attractive solution for data communication applications due to its advantageous performances especially at ultrahigh speeds that next-generation data communication systems demand.

3.6.5 $BaTiO_3$ on Si

With Pockels coefficients above $r > 1000$ pm/V [181], BTO is one of the materials with the strongest Pockels effect known today [182]. Because the intrinsic EO material properties are 30 times larger than in LN and because it is a solid-state crystal with better thermal and optical stability than organics, BTO became an attractive material for integrated optical modulators. Challenges in BTO such as strong off-axis tensor coefficients, multidomain structure, and integration as thin films into a photonic platform have, however, only recently been solved. In this section, we summarize the history of BTO modulators, the progress on components on silicon, and the integration of BTO with silicon photonics.

The first demonstration of waveguide-based modulators using BTO was made on magnesium oxide (MgO) substrates around the year 2000 [183,184]. The substrates enabled epitaxial growth of films via metal-organic chemical vapor deposition and pulsed laser deposition and ensured optical confinement in the BTO layer ($n \sim 2.3$) on top of MgO ($n \sim 1.7$). Epitaxial growth is required, first to obtain high-quality films with strong optical properties [185] and, second, to align the waveguides at specific angles relative to the BTO crystal, to exploit the strongest tensor elements [186]. The early work on MgO demonstrated the feasibility of realizing BTO-based integrated modulators, but the actual device performance was moderate ($V_\pi \sim 20-50$ V) due to large optical modes and limited material quality ($r \sim 50$ pm/V in Ref. [183]). In addition, the scalability to cost-efficient photonic platforms was unsolved due to the choice of substrates.

The development of high-quality, epitaxial BTO layers with strong Pockels coefficients on silicon ($r \sim 150$ pm/V) via molecular-beam epitaxy was reported in 2013 [187] (Fig. 3.26), and it enabled the integration of such high-Pockels material into silicon photonic platforms and reactivated research and development (R&D) activities on BTO modulators. Indeed, the first demonstrations of BTO-based passive waveguides [188] and modulators on silicon substrates followed quickly [189,190]. Waveguides were formed in an amorphous silicon layer on top of epitaxial BTO layers on silicon-on-insulator substrates, forming slot-waveguide structures (Fig. 3.27A). The modulator performance with $V_\pi L_\pi \sim 1.5$ V·cm exceeded many alternative modulator technologies, but bandwidth (<5 GHz) and losses (~50 dB/cm) represented limitations in that initial device generation. By adjusting process conditions and waveguide cross sections, the propagation losses were reduced to <3 dB/cm [191,192] in subsequent work. Indeed, moving away from high-capacitance slot-waveguide structures and optimizing mode overlap resulted in ring resonators with higher bandwidths of >30 GHz and better efficiency of $V_\pi L \sim 0.45$ V·cm [18] (Fig. 3.27B). Optical design optimizations were additionally supported by enhancing the properties of the films: bulk-like Pockels coefficients of $r > 900$ pm/V were reached in thin BTO films on silicon [18]. The field is working on further improvements of the device performance, in particular on reducing required voltages to <1 V, increasing the bandwidth to >100 GHz, and enabling broadband operation.

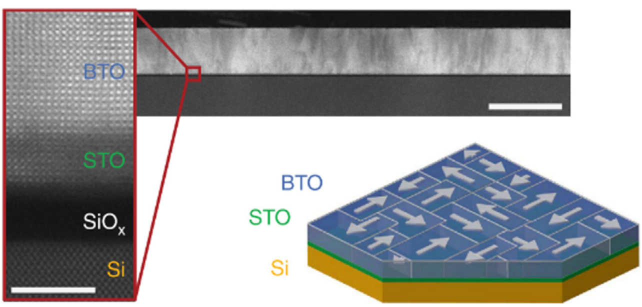

Figure 3.26 Fabrication of epitaxial BTO layers with strong Pockels effect directly on silicon wafers [187]. *BTO*, Barium titanate.
Source: From S. Abel et al., "A strong electro-optically active lead-free ferroelectric integrated on silicon," Nat. Commun., 4 (1) (2013) 1671.

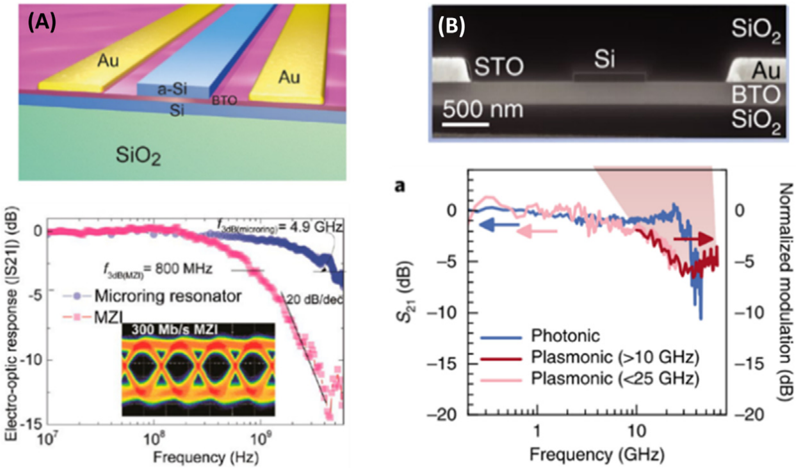

Figure 3.27 BTO-based optical modulators fabricated on silicon substrates with slot-waveguide (left [189]) and strip-loaded structures (right [18]). Please note that also the 3dB bandwidth of plasmonic modulators made from BTO is shown (see Ref. [18] for details). *BTO*, Barium titanate.
Source: From (left) C. Xiong et al., Active silicon integrated nanophotonics: ferroelectric $BaTiO_3$ devices, Nano Lett., 14 (3) (2014) 1419−1425; (right) S. Abel et al., "Large Pockels effect in micro- and nanostructured barium titanate integrated on silicon," Nat. Mater., 18 (1) (2019) 42−47.

These improvements require a coherent optimization of device designs and material stacks, taking into account optical, electro-optical, and RF properties.

Progress in the performance of individual devices fostered the development of integration concepts of the BTO technology into a scalable photonic platform. A particular target is to combine BTO-based Pockels modulators with standard silicon photonics since other devices such as detectors, passives, and couplers are readily available. Various integration routes such as deposition of films during the front-end-of-line (FEOL) process are in principle possible. One particular integration scheme has already been demonstrated: the integration of BTO modulators onto silicon photonic wafers during the back-end-of-line process [193] (Fig. 3.28), with two important results: first, the performance of FEOL silicon photonic structures is maintained in that integration process, as shown in high-speed germanium detectors as the typically most sensitive photonic component. Second, BTO-based modulators are indeed functional after the integration, with excellent $V_\pi L \sim 0.2\ \mathrm{V \cdot cm}$. Although BTO-integration schemes are not yet available in standard silicon photonic design and manufacturing routes, the first commercial development of BTO-based silicon photonics chips at scalable volumes has already been started [194].

Besides the target of reaching low-loss and high-speed Pockels modulators for communication, the strong EO effect has strong potential for other upcoming applications—in particular when available in a scalable, low-cost photonic platform. Examples of such new applications are nonvolatile optical memory elements [195],

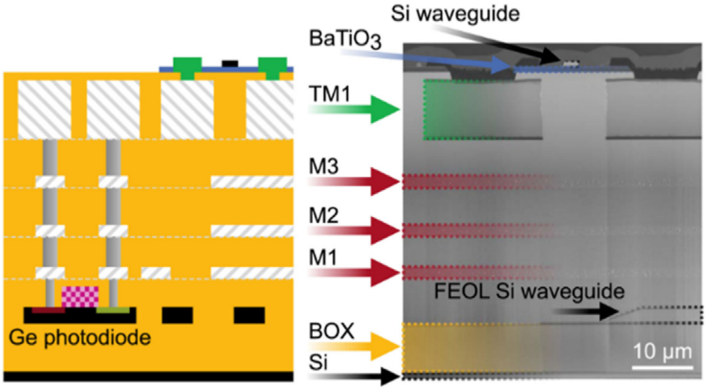

Figure 3.28 Example of the integration of BTO-based photonic modulators onto a silicon photonic platform. *BTO*, Barium titanate.
Source: From F. Eltes et al., A $BaTiO_3$-based electro-optic Pockels modulator monolithically integrated on an advanced silicon photonics platform, J. Light. Technol., 37 (5) (2019) 1456–1462.

ultracompact Pockels-based plasmonic modulators [18,196] (Fig. 3.27B), low-power tuning elements with three orders better power efficiency than traditional Joule heaters in silicon photonics [197], and efficient low-loss high-speed modulators operating at cryogenic temperatures for quantum transducers [192]. The rapid development of the photonic BTO technology with strong improvements in device performance within only a few years sets a promising outlook for having available a silicon photonic platform empowered with an ultrastrong Pockels effect.

3.7 Summary and perspectives

Silicon or silicon-compatible optical modulator is arguably the most researched of all silicon photonic devices. It has a storied 35-year history starting with Richard Soref and Brian Bennett's proposal in 1987 to use the FCPD effect for phase modulation in crystalline silicon [5]. Numerous silicon modulator designs were demonstrated in the years that followed, but they were limited in speed until the MOSCAP-based free-carrier dispersion device in 2004 showed >1 GHz bandwidth [36]. This seminal demonstration played a big part in igniting the explosion of silicon photonic R&D and investment across academia and industry. The result is a vibrant field of study with designs fueling optical transceivers in volume production now as well as designs promising orders of magnitude improvement in size, bandwidth density, and power consumption for future applications.

Today, the most proven high-speed silicon photonic modulators use the FCPD effect of reverse bias p-n diodes in the two branches of MZI designs. They support 25.78 Gbps NRZ, 53.125 Gbps PAM4, and 106.25 Gbps PAM4 modulation of datacom's optical pluggable multi source agreement (MSA) products. Similar designs are being developed for the next speed node of 212.5 Gbps PAM4. Besides speed scaling, bandwidth density and power are key performance drivers as the industry moves to pack more data into the same pluggable module form factors and, more aggressively, into much smaller copackage optics footprints, as discussed in Chapters 6 and 7. Ring resonator-based devices have the needed reduction in size, and designs using reverse bias p-n diodes or MOS capacitors for high-speed phase modulation have demonstrated good performance. So they are among the most promising modulators for next-generation datacom applications. Ge FKE and QCSE modulators also have the needed compact form factor, but they must demonstrate improved modulation efficiency in the O-band, which is the standard for datacom, and mature their material growth onto the silicon photonic platform before they can be viable for product.

The exponential growth of data, which is doubling every 2−3 years, demands similar rapid scaling of bandwidth density and power. To meet future performance targets, high-speed optical modulation requires disruptive innovation. As a result, there is a large body of research focused on integrating onto the silicon photonic platform materials with much better EO coefficients than silicon and germanium. III−V bonding onto Si to create a MOS capacitor device for modulation is a promising approach because of its demonstrated performance and its bonding, and integration process is similar to what has already been proven for hybrid laser integration, see Chapter 2. Integrating other materials like EO polymers, graphene, LN, $BaTiO_3$, etc. onto the silicon platform is also interesting because they have the potential to enable much more efficient and therefore more compact and lower power modulators than what is possible with native silicon designs. Nevertheless, their adoption for product will be critically dependent on our ability to overcome the complexity and cost of hybrid integration. While it is not clear which hybrid approach will ultimately surpass and displace proven silicon devices, the high-interest level and steady progress in this area underscore researchers' commitment to aggressively scale performance and are reasons for us to be hopeful that additional technology breakthroughs are in our near future.

References

[1] L. Vivien, L. Pavesi, vol. Chapter 9 Handbook of Silicon Photonics, Taylor & Francis, 2016.

[2] G. Cocorullo, F.G. Della Corte, I. Rendina, Temperature dependence of the thermo-optic coefficient in crystalline silicon between room temperature and 550 K at the wavelength of 1523 nm, Appl. Phys. Lett. 74 (22) (1999) 3338−3340. Available from: https://doi.org/10.1063/1.123337.

[3] D. Perez-Galacho, et al., Integrated polarization beam splitter for 100/400 GE polarization multiplexed coherent optical communications, J. Light. Technol. 32 (3) (2014) 361−368. Available from: https://doi.org/10.1109/JLT.2013.2293782.

[4] G.T. Reed (Ed.), Silicon Photonics: The State of the Art, John Wiley & Sons, Ltd, Chichester, UK, 2008.

[5] R. Soref, B. Bennett, Electrooptical effects in silicon, IEEE J. Quantum Electron. 23 (1) (1987) 123−129. Available from: https://doi.org/10.1109/JQE.1987.1073206.
[6] A. Frova, P. Handler, F.A. Germano, D.E. Aspnes, Electro-absorption effects at the band edges of silicon and germanium, Phys. Rev. 145 (2) (1966) 575−583. Available from: https://doi.org/10.1103/PhysRev.145.575.
[7] G.T. Reed, et al., Recent breakthroughs in carrier depletion based silicon optical modulators, Nanophotonics 3 (4−5) (2014) 229−245. Available from: https://doi.org/10.1515/nanoph-2013-0016.
[8] F.Y. Gardes, D.J. Thomson, N.G. Emerson, G.T. Reed, 40 Gb/s silicon photonics modulator for TE and TM polarisations, Opt. Express 19 (12) (2011) 11804. Available from: https://doi.org/10.1364/OE.19.011804.
[9] D. Marris-Morini, et al., Low loss 40 Gbit/s silicon modulator based on interleaved junctions and fabricated on 300 mm SOI wafers, Opt. Express 21 (19) (2013) 22471. Available from: https://doi.org/10.1364/OE.21.022471.
[10] Q. Xu, S. Manipatruni, B. Schmidt, J. Shakya, M. Lipson, 125 Gbit/s carrier-injection-based silicon micro-ring silicon modulators, Opt. Express 15 (2) (2007) 430. Available from: https://doi.org/10.1364/OE.15.000430.
[11] I. Charlet, Y. Desieres, D. Marris-Morini, F. Boeuf, Capacitive modulator design optimization using Si and strained-SiGe for datacom applications, IEEE J. Sel. Top. Quantum Electron. 27 (3) (2021) 1−8. Available from: https://doi.org/10.1109/JSTQE.2020.3028447.
[12] D. Galacho, High Speed Optical Modulation, Advanced Modulation Formats and Mode Division Multiplexing in Silicon Photonics, Université Paris-Saclay, 2016.
[13] L. Vivien et al., "Building Blocks of Silicon Photonics," Semiconductors and Semimetals, Elsevier, 101 (2019) 1−41.
[14] L. Mastronardi, et al., High-speed Si/GeSi hetero-structure electro absorption modulator, Opt. Express 26 (6) (2018) 6663. Available from: https://doi.org/10.1364/OE.26.006663.
[15] P. Chaisakul, et al., 23 GHz Ge/SiGe multiple quantum well electro-absorption modulator, Opt. Express 20 (3) (2012) 3219. Available from: https://doi.org/10.1364/OE.20.003219.
[16] M.-S. Rouifed, et al., Advances toward Ge/SiGe quantum-well waveguide modulators at 1.3 μm, IEEE J. Sel. Top. Quantum Electron. 20 (4) (2014) 33−39. Available from: https://doi.org/10.1109/JSTQE.2013.2294456.
[17] C. Wang, et al., Integrated lithium niobate electro-optic modulators operating at CMOS-compatible voltages, Nature 562 (7725) (2018) 101−104. Available from: https://doi.org/10.1038/s41586-018-0551-y.
[18] S. Abel, et al., Large Pockels effect in micro- and nanostructured barium titanate integrated on silicon, Nat. Mater. 18 (1) (2019) 42−47. Available from: https://doi.org/10.1038/s41563-018-0208-0.
[19] M. Berciano, et al., Fast linear electro-optic effect in a centrosymmetric semiconductor, Commun. Phys. 1 (1) (2018) 64. Available from: https://doi.org/10.1038/s42005-018-0064-x.
[20] D. Munk, et al., Surface acoustic wave photonic devices in silicon on insulator, Nat. Commun. 10 (1) (2019) 4214. Available from: https://doi.org/10.1038/s41467-019-12157-x.
[21] B.S. Dennis, M.I. Haftel, D.A. Czaplewski, D. Lopez, G. Blumberg, V.A. Aksyuk, Compact nanomechanical plasmonic phase modulators, Nat. Photonics 9 (4) (2015) 267−273. Available from: https://doi.org/10.1038/nphoton.2015.40.
[22] R.A. Soref, B.R. Bennett, "Kramers-Kronig Analysis of Electro-Optical Switching in Silicon," Mar. 1987, pp. 32. Available from: https://doi.org/10.1117/12.937193.

[23] J.P. Lorenzo, R.A. Soref, 1.3 μm electro-optic silicon switch, Appl. Phys. Lett. 51 (1) (1987) 6−8. Available from: https://doi.org/10.1063/1.98887.
[24] L. Friedman, R.A. Soref, J.P. Lorenzo, Silicon double-injection electro-optic modulator with junction gate control, J. Appl. Phys. 63 (6) (1988) 1831−1839. Available from: https://doi.org/10.1063/1.339878.
[25] C.K. Tang, G.T. Reed, A.J. Walton, A.G. Rickman, Simulation of a low loss optical modulator for fabrication in Simox material, MRS Proc. 298 (1993) 247. Available from: https://doi.org/10.1557/PROC-298-247.
[26] C.K. Tang, G.T. Reed, A.J. Walton, A.G. Rickman, Low-loss, single-model optical phase modulator in SIMOX material, J. Light. Technol. 12 (8) (1994) 1394−1400. Available from: https://doi.org/10.1109/50.317527.
[27] G.T. Reed, C.E. Jason Png, Silicon optical modulators, Mater. Today 8 (1) (2005) 40−50. Available from: https://doi.org/10.1016/S1369-7021(04)00678-9.
[28] A. Cutolo, M. Iodice, P. Spirito, L. Zeni, Silicon electro-optic modulator based on a three terminal device integrated in a low-loss single-mode SOI waveguide, J. Light. Technol. 15 (3) (1997) 505−518. Available from: https://doi.org/10.1109/50.557567.
[29] C.K. Tang, G.T. Reed, Highly efficient optical phase modulator in SOI waveguides, Electron. Lett. 31 (6) (1995) 451−452. Available from: https://doi.org/10.1049/el:19950328.
[30] S.M. Jackson, et al., Optical beamsteering using integrated optical modulators, J. Light. Technol. 15 (12) (1997) 2259−2263. Available from: https://doi.org/10.1109/50.643551.
[31] S.M. Jackson, et al., A novel optical phase modulator design suitable for phased arrays, J. Light. Technol. 16 (11) (1998) 2016−2019. Available from: https://doi.org/10.1109/50.730364.
[32] P.D. Hewitt, G.T. Reed, Improving the response of optical phase modulators in SOI by computer simulation, J. Light. Technol. 18 (3) (2000) 443−450. Available from: https://doi.org/10.1109/50.827519.
[33] P.D. Hewitt, G.T. Reed, Improved modulation performance of a silicon p-i-n device by trench isolation, J. Light. Technol. 19 (3) (2001) 387−390. Available from: https://doi.org/10.1109/50.918892.
[34] I. Day et al., "Tapered silicon waveguides for low insertion loss highly-efficient high-speed electronic variable optical attenuators," in: *Optical Fiber Communications Conference*, 2003, pp. 249−251, Available from: https://doi.org/10.1109/OFC.2003.1247634.
[35] P. Dainesi, et al., CMOS compatible fully integrated Mach-Zehnder interferometer in SOI technology, IEEE Photonics Technol. Lett. 12 (6) (2000) 660−662. Available from: https://doi.org/10.1109/68.849076.
[36] A. Liu, et al., A high-speed silicon optical modulator based on a metal−oxide−semiconductor capacitor, Nature 427 (6975) (2004) 615−618. Available from: https://doi.org/10.1038/nature02310.
[37] L. Liao, et al., High speed silicon Mach-Zehnder modulator, Opt. Express 13 (8) (2005) 3129. Available from: https://doi.org/10.1364/OPEX.13.003129.
[38] C.E. Png, S.P. Chan, S.T. Lim, G.T. Reed, Optical phase modulators for MHz and GHz modulation in silicon-on-insulator (SOI), J. Light. Technol. 22 (6) (2004) 1573−1582. Available from: https://doi.org/10.1109/JLT.2004.827655.
[39] Q. Xu, B. Schmidt, S. Pradhan, M. Lipson, Micrometre-scale silicon electro-optic modulator, Nature 435 (7040) (2005) 325−327. Available from: https://doi.org/10.1038/nature03569.
[40] F.Y. Gardes, G.T. Reed, N.G. Emerson, C.E. Png, A sub-micron depletion-type photonic modulator in silicon on insulator, Opt. Express 13 (22) (2005) 8845. Available from: https://doi.org/10.1364/OPEX.13.008845.

[41] A. Liu, et al., High-speed optical modulation based on carrier depletion in a silicon waveguide, Opt. Express 15 (2) (2007) 660. Available from: https://doi.org/10.1364/OE.15.000660.
[42] L. Liao, et al., 40 Gbit/s silicon optical modulator for high-speed applications, Electron. Lett. 43 (22) (2007) 1196. Available from: https://doi.org/10.1049/el:20072253.
[43] D.J. Thomson, et al., High contrast 40Gbit/s optical modulation in silicon, Opt. Express 19 (12) (2011) 11507. Available from: https://doi.org/10.1364/OE.19.011507.
[44] D.J. Thomson, et al., 50-Gb/s silicon optical modulator, IEEE Photonics Technol. Lett. 24 (4) (2012) 234−236. Available from: https://doi.org/10.1109/LPT.2011.2177081.
[45] K. Li, et al., Electronic−photonic convergence for silicon photonics transmitters beyond 100 Gbps on−off keying, Optica 7 (11) (2020) 1514. Available from: https://doi.org/10.1364/OPTICA.411122.
[46] M. Chagnon, et al., Design, analysis, and transmission system performance of a 41 GHz silicon photonic modulator, Opt. Express 23 (11) (2015) 14263. Available from: https://doi.org/10.1364/oe.23.014263.
[47] S. Meister, et al., Matching p-i-n-junctions and optical modes enables fast and ultra-small silicon modulators, Opt. Express 21 (13) (2013) 16210. Available from: https://doi.org/10.1364/OE.21.016210.
[48] S. Akiyama, et al., Compact PIN-diode-based silicon modulator using side-wall-grating waveguide, IEEE J. Sel. Top. Quantum Electron. 19 (6) (2013) 74−84. Available from: https://doi.org/10.1109/JSTQE.2013.2278438.
[49] A. Shakoor, K. Nozaki, E. Kuramochi, K. Nishiguchi, A. Shinya, M. Notomi, Compact 1D-silicon photonic crystal electro-optic modulator operating with ultra-low switching voltage and energy, Opt. Express 22 (23) (2014) 28623. Available from: https://doi.org/10.1364/OE.22.028623.
[50] Y. Sobu, G. Huang, S. Tanaka, Y. Tanaka, Y. Akiyama, T. Hoshida, High-speed optical digital-to-analog converter operation of compact two-segment all-silicon Mach−Zehnder modulator, J. Light. Technol. 39 (4) (2021) 1148−1154. Available from: https://doi.org/10.1109/JLT.2020.3035684.
[51] J. Van Campenhout, M. Pantouvaki, P. Verheyen, S. Selvaraja, G. Lepage, H. Yu, W. Lee, J. Wouters, D. Goossens, M. Moelants, W. Bogaerts, P. Absil, Low-voltage, low-loss, multi-Gb/s silicon micro-ring modulator based on a MOS capacitor, in: *OFC/NFOEC*, 2012, pp. 1−3.
[52] M. Webster et al., "An efficient MOS-capacitor based silicon modulator and CMOS drivers for optical transmitters," in: *11th International Conference on Group IV Photonics (GFP)*, Aug. 2014, pp. 1−2, Available from: https://doi.org/10.1109/JLT.2020.3035684.
[53] M. Sodagar, et al., Compact, 15 Gb/s electro-optic modulator through carrier accumulation in a hybrid Si/SiO_2/Si microdisk, Opt. Express 23 (22) (2015) 28306. Available from: https://doi.org/10.1364/OE.23.028306.
[54] K. Debnath, et al., All-silicon carrier accumulation modulator based on a lateral metal-oxide-semiconductor capacitor, Photonics Res. 6 (5) (2018) 373. Available from: https://doi.org/10.1364/PRJ.6.000373.
[55] W. Zhang, et al., High bandwidth capacitance efficient silicon MOS modulator, J. Light. Technol. 39 (1) (2021) 201−207. Available from: https://doi.org/10.1109/JLT.2020.3026945.
[56] M. Sakib et al., "A high-speed micro-ring modulator for next generation energy-efficient optical networks beyond 100 Gbaud," in: *Conference on Lasers and Electro-Optics*, 2021, pp. SF1C.3. Available from: https://doi.org/10.1364/CLEO_SI.2021.SF1C.3.

[57] W. Franz, Einfluß eines elektrischen Feldes auf eine optische Absorptionskante, Z. für Naturforsch. A 13 (6) (1958) 484−489. Available from: https://doi.org/10.1515/zna-1958-0609.
[58] L.V. Keldysh, Behavior of non-metallic crystals in strong electric fields, Sov. J. Exp. Theor. Phys. 6 (1958) 7631958, Accessed: Oct. 09, 2021. [Online]. Available. Available from: https://ui.adsabs.harvard.edu/abs/1958JETP . . ..6.0.763K/abstract.
[59] S. Jongthammanurak, et al., Large electro-optic effect in tensile strained Ge-on-Si films, Appl. Phys. Lett. 89 (16) (2006) 161115. Available from: https://doi.org/10.1063/1.2363948.
[60] C. Porret et al., "O-band GeSi quantum-confined stark effect electro-absorption modulator integrated in a 220nm silicon photonics platform," in: *2020 IEEE Symposium on VLSI Technology*, Jun. 2020, pp. 1−2. Available from: https://doi.org/10.1109/VLSITechnology18217.2020.9265082.
[61] P. Chaisakul et al., "High speed electro-absorption modulator based on quantum-confined stark effect from Ge/SiGe multiple quantum wells," in: *The 9th International Conference on Group IV Photonics (GFP)*, Aug. 2012, pp. 60−62. Available from: https://doi.org/10.1109/GROUP4.2012.6324086.
[62] E.H. Edwards, et al., Low-voltage broad-band electroabsorption from thin Ge/SiGe quantum wells epitaxially grown on silicon, Opt. Express 21 (1) (2013) 867. Available from: https://doi.org/10.1364/OE.21.000867.
[63] J.E. Roth, et al., C-band side-entry Ge quantum-well electroabsorption modulator on SOI operating at 1 V swing, Electron. Lett. 44 (1) (2008) 49. Available from: https://doi.org/10.1049/el:20082979.
[64] S. Ren, et al., Ge/SiGe quantum well waveguide modulator monolithically integrated with SOI waveguides, IEEE Photonics Technol. Lett. 24 (6) (2012) 461−463. Available from: https://doi.org/10.1109/LPT.2011.2181496.
[65] K. Zang, et al., Germanium quantum well QCSE waveguide modulator with tapered coupling in distributed modulator−detector system, J. Light. Technol. 35 (21) (2017) 4629−4633. Available from: https://doi.org/10.1109/JLT.2017.2753582.
[66] L. Mastronardi, GeSi Franz-Keldysh modulator for silicon photonic integrated circuits (Doctoral thesis), University of Southampton, 2019. <https://scholar.google.co.uk/scholar?hl = en&as_sdt = 0%2C5&q = GeSi + Franz-Keldysh + modulator + for + silicon + photonic + integrated + circuits&btnG = > (accessed 09.10.21).
[67] Y.-H. Kuo, et al., Quantum-confined stark effect in Ge/SiGe quantum wells on Si for optical modulators, IEEE J. Sel. Top. Quantum Electron. 12 (6) (2006) 1503−1513. Available from: https://doi.org/10.1109/JSTQE.2006.883146.
[68] A.E.-J. Lim, et al., Novel evanescent-coupled germanium electro-absorption modulator featuring monolithic integration with germanium p-i-n photodetector, Opt. Express 19 (6) (2011) 5040. Available from: https://doi.org/10.1364/OE.19.005040.
[69] S.A. Srinivasan, et al., 56 Gb/s germanium waveguide electro-absorption modulator, J. Light. Technol. 34 (2) (2016) 419−424. Available from: https://doi.org/10.1109/JLT.2015.2478601.
[70] J. Liu, et al., Waveguide-integrated, ultralow-energy GeSi electro-absorption modulators, Nat. Photonics 2 (7) (2008) 433−437. Available from: https://doi.org/10.1038/nphoton.2008.99.
[71] D. Feng, et al., High-speed GeSi electroabsorption modulator on the SOI waveguide platform, IEEE J. Sel. Top. Quantum Electron. 19 (6) (2013) 64−73. Available from: https://doi.org/10.1109/JSTQE.2013.2278881.
[72] A.V. Krishnamoorthy, et al., A low-power, high-speed, 9-channel germanium-silicon electro-absorption modulator array integrated with digital CMOS driver and wavelength

multiplexer, Opt. Express 22 (10) (2014) 12289−12295. Available from: https://doi.org/10.1364/OE.22.012289.

[73] O. El-Aassar, G.M. Rebeiz, A DC-to-108-GHz CMOS SOI distributed power amplifier and modulator driver leveraging multi-drive complementary stacked cells, IEEE J. Solid-State Circuits 54 (12) (2019) 3437−3451. Available from: https://doi.org/10.1109/JSSC.2019.2941013.

[74] Y. Zhao, L. Vera, J.R. Long, A 10 Gb/s, 6 V p-p, digitally controlled, differential distributed amplifier MZM driver, IEEE J. Solid-State Circuits 49 (9) (2014) 2030−2043. Available from: https://doi.org/10.1109/JSSC.2014.2327036.

[75] J. Kim, J.F. Buckwalter, A 40-Gb/s optical transceiver front-end in 45 nm SOI CMOS, IEEE J. Solid-State Circuits 47 (3) (2012) 615−626. Available from: https://doi.org/10.1109/JSSC.2011.2178723.

[76] D.-U. Li, C.-M. Tsai, 10-Gb/s modulator drivers with local feedback networks, IEEE J. Solid-State Circuits 41 (5) (2006) 1025−1030. Available from: https://doi.org/10.1109/JSSC.2006.872878.

[77] H. Li, et al., A 112 Gb/s PAM4 silicon photonics transmitter with microring modulator and CMOS driver, J. Light. Technol. 38 (1) (2020) 131−138. Available from: https://doi.org/10.1109/JLT.2019.2938731.

[78] C. Xiong, D.M. Gill, J.E. Proesel, J.S. Orcutt, W. Haensch, W.M.J. Green, Monolithic 56 Gb/s silicon photonic pulse-amplitude modulation transmitter, Optica 3 (10) (2016) 1060. Available from: https://doi.org/10.1364/OPTICA.3.001060.

[79] Q. Liao et al., "A 50Gb/s high-efficiency Si-photonic transmitter with lump-segmented MZM and integrated PAM4 CDR," in: *2021 IEEE Custom Integrated Circuits Conference (CICC)*, Apr. 2021, pp. 1−2. Available from: https://doi.org/10.1109/CICC51472.2021.9431546.

[80] H. Li, et al., A 3-D-integrated silicon photonic microring-based 112-Gb/s PAM-4 transmitter with nonlinear equalization and thermal control, IEEE J. Solid-State Circuits 56 (1) (2021) 19−29. Available from: https://doi.org/10.1109/JSSC.2020.3022851.

[81] M. Kim, D.-H. Kwon, D.-W. Rho, W.-Y. Choi, A low-power 28-Gb/s PAM-4MZM driver with level pre-distortion, IEEE Trans. Circuits Syst. II Express Briefs 68 (3) (2021) 908−912. Available from: https://doi.org/10.1109/TCSII.2020.3020128.

[82] C. Li, et al., Silicon photonic transceiver circuits with microring resonator bias-based wavelength stabilization in 65 nm CMOS, IEEE J. Solid-State Circuits 49 (6) (2014) 1419−1436. Available from: https://doi.org/10.1109/JSSC.2014.2321574.

[83] S. Shopov, S.P. Voinigescu, A 3 × 60Gb/s transmitter/repeater front-end with 4.3VPP single-ended output swing in a 28nm UTBB FD-SOI technology, IEEE J. Solid-State Circuits 51 (7) (2016) 1651−1662. Available from: https://doi.org/10.1109/JSSC.2016.2545703.

[84] N. Qi, et al., Co-design and demonstration of a 25-Gb/s silicon-photonic Mach−Zehnder modulator with a CMOS-based high-swing driver, IEEE J. Sel. Top. Quantum Electron. 22 (6) (2016) 131−140. Available from: https://doi.org/10.1109/JSTQE.2016.2602102.

[85] T. Jyo, M. Nagatani, J. Ozaki, M. Ishikawa, H. Nosaka, 12.3 A 48GHz BW 225mW/ch linear driver IC with stacked current-reuse architecture in 65nm CMOS for beyond-400Gb/s coherent optical transmitters, in: *2020 IEEE International Solid- State Circuits Conference - (ISSCC)*, 2020, pp. 212−214. Available from: https://doi.org/10.1109/ISSCC19947.2020.9063027.

[86] K. Li et al., "Co-design of electronics and photonics components for silicon photonics transmitters," in: *2018 European Conference on Optical Communication (ECOC)*, Sep. 2018, pp. 1−3. Available from: https://doi.org/10.1109/ECOC.2018.8535212.

[87] D. Petousi, et al., Monolithically integrated high-extinction-ratio MZM with a segmented driver in photonic BiCMOS, IEEE Photonics Technol. Lett. 28 (24) (2016) 2866−2869. Available from: https://doi.org/10.1109/LPT.2016.2624700.

[88] T.N. Huynh, et al., Flexible transmitter employing silicon-segmented Mach−Zehnder modulator with 32-nm CMOS distributed driver, J. Light. Technol. 34 (22) (2016) 5129−5136. Available from: https://doi.org/10.1109/JLT.2016.2606558.

[89] H. Sepehrian, A. Yekani, L.A. Rusch, W. Shi, CMOS-photonics codesign of an integrated DAC-Less PAM-4 silicon photonic transmitter, IEEE Trans. Circuits Syst. I Regul. Pap. 63 (12) (2016) 2158−2168. Available from: https://doi.org/10.1109/TCSI.2016.2613514.

[90] P. Rito, et al., A monolithically integrated segmented linear driver and modulator in EPIC 0.25- μ m SiGe:C BiCMOS platform, IEEE Trans. Microw. Theory Tech. 64 (12) (2016) 4561−4572. Available from: https://doi.org/10.1109/TMTT.2016.2618392.

[91] Ch. Jany, Ch. Kazmierski, J. Decobert, F. Alexandre, F. Blache, O. Drisse, D. Carpentier, N. Lagay, F. Martin, E. Derouin, T. Johansen, Ch. Jiang, Semi-insulating buried heterostructure 1.55 micrometer InGaAlAs electroabsorption modulated laser with 60GHz bandwidth, in: *33rd European Conference and Exhibition of Optical Communication − post-deadline papers*, 16−20 September 2007.

[92] Y. Tang, J.D. Peters, J.E. Bowers, Over 67 GHz bandwidth hybrid silicon electroabsorption modulator with asymmetric segmented electrode for 13 μm transmission, Opt. Express 20 (10) (2012) 11529. Available from: https://doi.org/10.1364/OE.20.011529.

[93] M.R. Gokhale, P.V. Studenkov, J. Ueng-McHale, J. Thomson, J. Yao, Uncooled, 10Gb/s 1310 nm electroabsorption modulated laser, Opt. Fiber Commun. Conf. Opt. Soc. Am. (2021). p. PD42, 2003, Accessed: Oct. 10. Available from: https://www.osa-publishing.org/abstract.cfm?uri = ofc-2003-PD42.

[94] W. Kobayashi, et al., Wide temperature range (-25 degrees C-100 degrees C) operation of a 10-Gb/s 1.55-mu m electroabsorption modulator integrated DFB laser for 80-km SMF transmission, IEEE Photonics Technol. Lett. 21 (15) (2009) 1054−1056. Available from: https://doi.org/10.1109/LPT.2009.2022182.

[95] H. Mardoyan et al., "204-GBaud on-off keying transmitter for inter-data center communications," in: *Optical Fiber Communication Conference Postdeadline Papers*, 2018, p. Th4A.4. Available from: https://doi.org/10.1364/OFC.2018.Th4A.4.

[96] K. Zhong, et al., 140-Gb/s 20-km transmission of PAM-4 signal at 1.3 μm for short reach communications, IEEE Photonics Technol. Lett. 27 (16) (2015) 1757−1760. Available from: https://doi.org/10.1109/LPT.2015.2439571.

[97] U. Troppenz et al., "1.3 μm electroabsorption modulated lasers for PAM4/PAM8 single channel 100 Gb/s," in: *26th International Conference on Indium Phosphide and Related Materials (IPRM)*, 2014, pp. 1−2. Available from: https://doi.org/10.1109/ICIPRM.2014.6880562.

[98] W. Kobayashi, et al., Novel approach for chirp and output power compensation applied to a 40-Gbit/s EADFB laser integrated with a short SOA, Opt. Express 23 (7) (2015) 9533. Available from: https://doi.org/10.1364/OE.23.009533.

[99] S. Kanazawa, et al., Flip-chip interconnection lumped-electrode EADFB laser for 100-Gb/s/ λ transmitter, IEEE Photonics Technol. Lett. 27 (16) (2015) 1699−1701. Available from: https://doi.org/10.1109/LPT.2015.2438076.

[100] S. Kanazawa, et al., 214-Gb/s 4-PAM operation of flip-chip interconnection EADFB Laser module, J. Light. Technol. 35 (3) (2017) 418−422. Available from: https://doi.org/10.1109/JLT.2016.2632164.

[101] X. Wu et al., A 20Gb/s NRZ/PAM-4 1V transmitter in 40nm CMOS driving a Si-photonic modulator in 0.13 μm CMOS, in: *2013 IEEE International Solid-State Circuits Conference Digest of Technical Papers*, Feb. 2013, pp. 128−129. Available from: https://doi.org/10.1109/ISSCC.2013.6487667.

[102] Y. Ogiso, et al., Over 67 GHz bandwidth and 1.5 V V_{π} InP-based optical IQ modulator with n-i-p-n heterostructure, J. Light. Technol. 35 (8) (2017) 1450−1455. Available from: https://doi.org/10.1109/JLT.2016.2639542.

[103] Y. Ogiso et al., "Ultra-high bandwidth InP IQ modulators for next generation coherent transmitter," in: *2017 IEEE Compound Semiconductor Integrated Circuit Symposium (CSICS)*, Oct. 2017, pp. 1−4. Available from: https://doi.org/10.1109/CSICS.2017.8240423.

[104] K. Prosyk et al., "Tunable InP-based optical IQ modulator for 160 Gb/s," in: *37th European Conference and Exposition on Optical Communications*, 2011, pp. Th.13.A.5. Available from: https://doi.org/10.1364/ECOC.2011.Th.13.A.5.

[105] E. Yamada et al., "112-Gb/s InP DP-QPSK modulator integrated with a Silica-PLC polarization multiplexing circuit," in: *Proc. OFC, National Fiber Optic Engineers Conference*, 2012, pp. PDP5A.9. Available from: https://doi.org/10.1364/NFOEC.2012.PDP5A.9.

[106] K. Tsuzuki, et al., 40 Gbit/s n−i−n InP Mach−Zehnder modulator with a voltage of 2.2 V, Electron. Lett. 39 (20) (2003) 1464. Available from: https://doi.org/10.1049/el:20030939.

[107] F. Tsuzuki, T. Ishibashi, T. Ito, N. Kikuchi, F. Kano, 80 Gb/s InP Mach-Zehnder modulator module using liquid crystal polymer (LCP) transmission nine, in: *35th European Conference on Optical Communication*, 20−24 September 2009.

[108] S. Matsuo, T. Fujii, K. Hasebe, K. Takeda, T. Sato, T. Kakitsuka, Directly modulated buried heterostructure DFB laser on SiO_2/Si substrate fabricated by regrowth of InP using bonded active layer, Opt. Express 22 (10) (2014) 12139. Available from: https://doi.org/10.1364/OE.22.012139.

[109] S. Matsuo, T. Fujii, K. Hasebe, K. Takeda, T. Sato, T. Kakitsuka, Directly modulated DFB Laser on SiO_2/Si substrate for datacenter networks, J. Light. Technol. 33 (6) (2015) 1217−1222. Available from: https://doi.org/10.1109/JLT.2014.2386875.

[110] S. Matsuo, T. Kakitsuka, Low-operating-energy directly modulated lasers for short-distance optical interconnects, Adv. Opt. Photonics 10 (3) (2018) 567. Available from: https://doi.org/10.1364/AOP.10.000567.

[111] T. Fujii, et al., Heterogeneously integrated membrane lasers on Si substrate for low operating energy optical links, IEEE J. Sel. Top. Quantum Electron. 24 (1) (2018) 1−8. Available from: https://doi.org/10.1109/JSTQE.2017.2778510.

[112] H. Nishi, et al., Integration of eight-channel directly modulated membrane-laser array and SiN AWG multiplexer on Si, J. Light. Technol. 37 (2) (2019) 266−273. Available from: https://doi.org/10.1109/JLT.2018.2873742.

[113] T. Fujii, et al., Development of an epitaxial growth technique using III-V on a Si platform for heterogeneous integration of membrane photonic devices on Si, Appl. Sci. 11 (4) (2021) 1801. Available from: https://doi.org/10.3390/app11041801.

[114] T. Hiraki, et al., Integration of a high-efficiency Mach-Zehnder modulator with a DFB laser using membrane InP-based devices on a Si photonics platform, Opt. Express 29 (2) (2021) 2431. Available from: https://doi.org/10.1364/OE.411483.

[115] H.-W. Chen, J.D. Peters, J.E. Bowers, Forty Gb/s hybrid silicon Mach-Zehnder modulator with low chirp, Opt. Express 19 (2) (2011) 1455. Available from: https://doi.org/10.1364/OE.19.001455.

[116] H.-W. Chen, High-Speed Hybrid Silicon Mach-Zehnder Modulator and Tunable Microwave Filter, University of California, Santa Barbara, 2011.
[117] D. Liang, J.E. Bowers, Recent progress in heterogeneous III-V-on-silicon photonic integration, Light. Adv. Manuf. 2 (1) (2021) 1–25. Available from: https://doi.org/10.37188/lam.2021.005.
[118] D. Liang, X. Huang, G. Kurczveil, M. Fiorentino, R.G. Beausoleil, Integrated finely tunable microring laser on silicon, Nat. Photonics 10 (11) (2016) 719–722. Available from: https://doi.org/10.1038/nphoton.2016.163.
[119] T. Hiraki, et al., Heterogeneously integrated III–V/Si MOS capacitor Mach–Zehnder modulator, Nat. Photonics 11 (8) (2017) 482–485. Available from: https://doi.org/10.1038/nphoton.2017.120.
[120] L. Dalton, S. Benight, Theory-guided design of organic electro-optic materials and devices, Polym. (Basel) 3 (3) (2011) 1325–1351. Available from: https://doi.org/10.3390/polym3031325.
[121] T. Baehr-Jones, et al., Optical modulation and detection in slotted silicon waveguides, Opt. Express 13 (14) (2005) 5216. Available from: https://doi.org/10.1364/OPEX.13.005216.
[122] C. Koos, et al., Silicon-organic hybrid (SOH) and plasmonic-organic hybrid (POH) integration, J. Light. Technol. 34 (2) (2016) 256–268. Available from: https://doi.org/10.1109/JLT.2015.2499763.
[123] C. Koos, et al., All-optical high-speed signal processing with silicon–organic hybrid slot waveguides, Nat. Photonics 3 (4) (2009) 216–219. Available from: https://doi.org/10.1038/nphoton.2009.25.
[124] D. Korn, et al., Lasing in silicon–organic hybrid waveguides, Nat. Commun. 7 (1) (2016) 10864. Available from: https://doi.org/10.1038/ncomms10864.
[125] D. Kohler, et al., Biophotonic sensors with integrated Si3N4-organic hybrid (SiNOH) lasers for point-of-care diagnostics, Light. Sci. Appl. 10 (1) (2021) 64. Available from: https://doi.org/10.1038/s41377-021-00486-w.
[126] V.R. Almeida, Q. Xu, C.A. Barrios, M. Lipson, Guiding and confining light in void nanostructure, Opt. Lett. 29 (11) (2004) 1209. Available from: https://doi.org/10.1364/OL.29.001209.
[127] C. Koos, L. Jacome, C. Poulton, J. Leuthold, W. Freude, Nonlinear silicon-on-insulator waveguides for all-optical signal processing, Opt. Express 15 (10) (2007) 5976. Available from: https://doi.org/10.1364/OE.15.005976.
[128] O. Marshall, M. Hsu, Z. Wang, B. Kunert, C. Koos, D. Van Thourhout, Heterogeneous integration on silicon photonics, Proc. IEEE 106 (12) (2018) 2258–2269. Available from: https://doi.org/10.1109/JPROC.2018.2858542.
[129] S. Koeber, et al., Femtojoule electro-optic modulation using a silicon–organic hybrid device, Light. Sci. Appl. 4 (2) (2015) e255. Available from: https://doi.org/10.1038/lsa.2015.28. e255.
[130] C. Kieninger, et al., Ultra-high electro-optic activity demonstrated in a silicon-organic hybrid modulator, Optica 5 (6) (2018) 739. Available from: https://doi.org/10.1364/OPTICA.5.000739.
[131] M. Lauermann, et al., Low-power silicon-organic hybrid (SOH) modulators for advanced modulation formats, Opt. Express 22 (24) (2014) 29927. Available from: https://doi.org/10.1364/OE.22.029927.
[132] S. Wolf, et al., DAC-Less amplifier-less generation and transmission of QAM signals using sub-volt silicon-organic hybrid modulators, J. Light. Technol. 33 (7) (2015) 1425–1432. Available from: https://doi.org/10.1109/JLT.2015.2394511.

[133] H. Zwickel, et al., Silicon-organic hybrid (SOH) modulators for intensity-modulation / direct-detection links with line rates of up to 120 Gbit/s, Opt. Express 25 (20) (2017) 23784. Available from: https://doi.org/10.1364/OE.25.023784.
[134] S. Wolf, et al., Silicon-organic hybrid (SOH) Mach-Zehnder modulators for 100 Gbit/s on-off Keying, Sci. Rep. 8 (1) (2018) 2598. Available from: https://doi.org/10.1038/s41598-017-19061-8.
[135] C. Kieninger, et al., Silicon-organic hybrid (SOH) Mach-Zehnder modulators for 100 GBd PAM4 signaling with sub-1 dB phase-shifter loss, Opt. Express 28 (17) (2020) 24693. Available from: https://doi.org/10.1364/OE.390315.
[136] M. Lauermann, et al., 40 GBd 16QAM Signaling at 160 Gb/s in a silicon-organic hybrid modulator, J. Light. Technol. 33 (6) (2015) 1210−1216. Available from: https://doi.org/10.1109/JLT.2015.2394211.
[137] S. Wolf, et al., Coherent modulation up to 100 GBd 16QAM using silicon-organic hybrid (SOH) devices, Opt. Express 26 (1) (2018) 220. Available from: https://doi.org/10.1364/OE.26.000220.
[138] C. Weimann, et al., Silicon-organic hybrid (SOH) frequency comb sources for terabit/s data transmission, Opt. Express 22 (3) (2014) 3629. Available from: https://doi.org/10.1364/OE.22.003629.
[139] M. Lauermann, et al., Integrated optical frequency shifter in silicon-organic hybrid (SOH) technology, Opt. Express 24 (11) (2016) 11694. Available from: https://doi.org/10.1364/OE.24.011694.
[140] H. Zwickel, et al., Verified equivalent-circuit model for slot-waveguide modulators, Opt. Express 28 (9) (2020) 12951. Available from: https://doi.org/10.1364/OE.383120.
[141] S. Ummethala, et al., THz-to-optical conversion in wireless communications using an ultra-broadband plasmonic modulator, Nat. Photonics 13 (8) (2019) 519−524. Available from: https://doi.org/10.1038/s41566-019-0475-6.
[142] M. Burla, et al., 500 GHz plasmonic Mach-Zehnder modulator enabling sub-THz microwave photonics, APL Photonics 4 (5) (2019) 056106. Available from: https://doi.org/10.1063/1.5086868.
[143] S. Ummethala, et al., Hybrid electro-optic modulator combining silicon photonic slot waveguides with high-k radio-frequency slotlines, Optica 8 (4) (2021) 511. Available from: https://doi.org/10.1364/OPTICA.411161.
[144] L. Dalton, M. Lauermann, C. Koos, in: Fundamental Aspects of Materials and Applications, 2, World Scienific, 2016, pp. 369−396.
[145] P.A. G. J. Sullivan, L.R. Dalton, D.L. Andrews, The materials genome for organic electro-optics and silicon/plasmonic—organic hybrid technologyin N. Horiz. Nanosci. Eng. (2015) 233−284.
[146] L.E. Johnson, L.R. Dalton, B.H. Robinson, Optimizing calculations of electronic excitations and relative hyperpolarizabilities of electrooptic chromophores, Acc. Chem. Res. 47 (11) (2014) 3258−3265. Available from: https://doi.org/10.1021/ar5000727.
[147] L.R. Dalton, P. Gunter, M. Jazbinsek, O.-P. Kwon, P.A. Sullivan, Organic Electro-Optics and Photonics, Cambridge University Press, Cambridge, 2015.
[148] W. Jin, et al., Benzocyclobutene barrier layer for suppressing conductance in nonlinear optical devices during electric field poling, Appl. Phys. Lett. 104 (24) (2014) 243304. Available from: https://doi.org/10.1063/1.4884829.
[149] C. Kieninger, et al., Demonstration of long-term thermally stable silicon-organic hybrid modulators at 85°C, Opt. Express 26 (21) (2018) 27955. Available from: https://doi.org/10.1364/OE.26.027955.

[150] A.K. Bodenmann, A.H. MacDonald, Graphene: exploring carbon flatland, Phys. Today 60 (8) (2007) 35−41. Available from: https://doi.org/10.1063/1.2774096.
[151] F. Bonaccorso, Z. Sun, T. Hasan, A.C. Ferrari, Graphene photonics and optoelectronics, Nat. Photonics 4 (9) (2010) 611−622. Available from: https://doi.org/10.1038/nphoton.2010.186.
[152] M. Romagnoli, et al., Graphene-based integrated photonics for next-generation datacom and telecom, Nat. Rev. Mater. 3 (10) (2018) 392−414. Available from: https://doi.org/10.1038/s41578-018-0040-9.
[153] M. Liu, et al., A graphene-based broadband optical modulator, Nature 474 (7349) (2011) 64−67. Available from: https://doi.org/10.1038/nature10067.
[154] M. Liu, X. Yin, X. Zhang, Double-layer graphene optical modulator, Nano Lett. 12 (3) (2012) 1482−1485. Available from: https://doi.org/10.1021/nl204202k.
[155] Y. Hu, et al., Broadband 10 Gb/s operation of graphene electro-absorption modulator on silicon, Laser Photon. Rev. 10 (2) (2016) 307−316. Available from: https://doi.org/10.1002/lpor.201500250.
[156] C. Alessandri, et al., High speed graphene-silicon electro-absorption modulators for the O-band and C-band, Jpn. J. Appl. Phys. 59 (5) (2020) 052008. Available from: https://doi.org/10.35848/1347-4065/ab8920.
[157] C.T. Phare, Y.-H. Daniel Lee, J. Cardenas, M. Lipson, Graphene electro-optic modulator with 30 GHz bandwidth, Nat. Photonics 9 (8) (2015) 511−514. Available from: https://doi.org/10.1038/nphoton.2015.122.
[158] R. Safian, M. Teng, L. Zhuang, S. Chakravarty, Foundry-compatible thin film lithium niobate modulator with RF electrodes buried inside the silicon oxide layer of the SOI wafer, Opt. Express 28 (18) (2020) 25843. Available from: https://doi.org/10.1364/OE.396335.
[159] M.A. Giambra, et al., High-speed double layer graphene electro-absorption modulator on SOI waveguide, Opt. Express 27 (15) (2019) 20145. Available from: https://doi.org/10.1364/OE.27.020145.
[160] H. Agarwal, et al., 2D-3D integration of hexagonal boron nitride and a high-κ dielectric for ultrafast graphene-based electro-absorption modulators, Nat. Commun. 12 (1) (2021) 1070. Available from: https://doi.org/10.1038/s41467-021-20926-w.
[161] V. Sorianello, G. Contestabile, M. Romagnoli, Graphene on silicon modulators, J. Light. Technol. 38 (10) (2020) 2782−2789. Available from: https://doi.org/10.1109/JLT.2020.2974189.
[162] V. Sorianello, et al., Graphene−silicon phase modulators with gigahertz bandwidth, Nat. Photonics 12 (1) (2018) 40−44. Available from: https://doi.org/10.1038/s41566-017-0071-6.
[163] T. Cusati, et al., Electrical properties of graphene-metal contacts, Sci. Rep. 7 (1) (2017) 5109. Available from: https://doi.org/10.1038/s41598-017-05069-7.
[164] H.-Y. Park, et al., Extremely low contact resistance on graphene through n-type doping and edge contact design, Adv. Mater. 28 (5) (2016) 864−870. Available from: https://doi.org/10.1002/adma.201503715.
[165] M.A. Giambra, et al., Wafer-scale integration of graphene-based photonic devices, ACS Nano 15 (2) (2021) 3171−3187. Available from: https://doi.org/10.1021/acsnano.0c09758.
[166] E.L. Wooten, et al., A review of lithium niobate modulators for fiber-optic communications systems, IEEE J. Sel. Top. Quantum Electron. 6 (1) (2000) 69−82. Available from: https://doi.org/10.1109/2944.826874.
[167] M. Zhang, C. Wang, P. Kharel, D. Zhu, M. Lončar, Integrated lithium niobate electro-optic modulators: when performance meets scalability, Optica 8 (5) (2021) 652. Available from: https://doi.org/10.1364/OPTICA.415762.

[168] A. Rao, S. Fathpour, Compact lithium niobate electrooptic modulators, IEEE J. Sel. Top. Quantum Electron. 24 (4) (2018) 1−14. Available from: https://doi.org/10.1109/JSTQE.2017.2779869.

[169] X. Chen et al., "Single-wavelength and single-photodiode 700 Gb/s entropy-loaded PS-256-QAM and 200-GBaud PS-PAM-16 Transmission over 10-km SMF," in: *2020 European Conference on Optical Communications (ECOC)*, Dec. 2020, pp. 1−4. Available from: https://doi.org/10.1109/ECOC48923.2020.9333201.

[170] Chen, G. Raybon, D. Che, J. Cho, K. W. Kim, "Transmission of 200-GBaud PDM probabilistically shaped 64-QAM signals modulated via a 100-GHz thin-film LiNbO3 I/Q modulator, in: *2021 Optical Fiber Communications Conference*, 2021, pp. 1−3.

[171] A.J. Mercante, S. Shi, P. Yao, L. Xie, R.M. Weikle, D.W. Prather, Thin film lithium niobate electro-optic modulator with terahertz operating bandwidth, Opt. Express 26 (11) (2018) 14810. Available from: https://doi.org/10.1364/OE.26.014810.

[172] M. Zhang, C. Wang, R. Cheng, A. Shams-Ansari, M. Lončar, Monolithic ultra-high-Q lithium niobate microring resonator, Optica 4 (12) (2017) 1536. Available from: https://doi.org/10.1364/OPTICA.4.001536.

[173] I. Krasnokutska, J.-L.J. Tambasco, X. Li, A. Peruzzo, Ultra-low loss photonic circuits in lithium niobate on insulator, Opt. Express 26 (2) (2018) 897. Available from: https://doi.org/10.1364/OE.26.000897.

[174] R. Wu, et al., Lithium niobate micro-disk resonators of quality factors above 10 7, Opt. Lett. 43 (17) (2018) 4116. Available from: https://doi.org/10.1364/OL.43.004116.

[175] M. Doi, M. Sugiyama, K. Tanaka, M. Kawai, Advanced LiNbO/sub 3/optical modulators for broadband optical communications, IEEE J. Sel. Top. Quantum Electron. 12 (4) (2006) 745−750. Available from: https://doi.org/10.1109/JSTQE.2006.876192.

[176] M. Xu, et al., High-performance coherent optical modulators based on thin-film lithium niobate platform, Nat. Commun. 11 (1) (2020) 3911. Available from: https://doi.org/10.1038/s41467-020-17806-0.

[177] N. Boynton, et al., A heterogeneously integrated silicon photonic/lithium niobate travelling wave electro-optic modulator, Opt. Express 28 (2) (2020) 1868. Available from: https://doi.org/10.1364/OE.28.001868.

[178] P. Ying, et al., Low-loss edge-coupling thin-film lithium niobate modulator with an efficient phase shifter, Opt. Lett. 46 (6) (2021) 1478. Available from: https://doi.org/10.1364/OL.418996.

[179] K. Luke, P. Kharel, C. Reimer, L. He, M. Loncar, M. Zhang, Wafer-scale low-loss lithium niobate photonic integrated circuits, Opt. Express 28 (17) (2020) 24452. Available from: https://doi.org/10.1364/OE.401959.

[180] M. Xu, M. He, X. Cai, Generation of flat optical frequency comb using integrated cascaded lithium niobate modulators, in: *Conference on Lasers and Electro-Optics*, 2020, p. STh1O.5. Available from: https://doi.org/10.1364/CLEO_SI.2020.STh1O.5.

[181] A.R. Johnston, J.M. Weingart, Determination of the low-frequency linear electro-optic effect in tetragonal $BaTiO_3$†, J. Opt. Soc. Am. 55 (7) (1965) 828. Available from: https://doi.org/10.1364/JOSA.55.000828.

[182] S. Abel, J. Fompeyrine, Electro-optically active oxides on silicon for photonics, in Thin Films on Silicon (Material Energy), 8, World Scientific, Singapore, 2016, pp. 455−501.

[183] D.M. Gill, C.W. Conrad, G. Ford, B.W. Wessels, S.T. Ho, Thin-film channel waveguide electro-optic modulator in epitaxial $BaTiO_3$, Appl. Phys. Lett. 71 (13) (1997) 1783−1785. Available from: https://doi.org/10.1063/1.119397.

[184] A. Petraru, J. Schubert, M. Schmid, C. Buchal, Ferroelectric $BaTiO_3$ thin-film optical waveguide modulators, Appl. Phys. Lett. 81 (8) (2002) 1375–1377. Available from: https://doi.org/10.1063/1.1498151.
[185] K.J. Kormondy, et al., Microstructure and ferroelectricity of $BaTiO_3$ thin films on Si for integrated photonics, Nanotechnology 28 (7) (2017) 075706. Available from: https://doi.org/10.1088/1361-6528/aa53c2.
[186] P. Castera, et al., Electro-optical modulation based on Pockels effect in $BaTiO_3$ with a multi-domain structure, IEEE Photonics Technol. Lett. 28 (9) (2016) 990–993. Available from: https://doi.org/10.1109/LPT.2016.2522509.
[187] S. Abel, et al., A strong electro-optically active lead-free ferroelectric integrated on silicon, Nat. Commun. 4 (1) (2013) 1671. Available from: https://doi.org/10.1038/ncomms2695.
[188] S. Abel et al., "Electro-optical properties of barium titanate films epitaxially grown on silicon," 2012, pp. 82630Y. Available from: https://doi.org/10.1117/12.908772.
[189] C. Xiong, et al., Active silicon integrated nanophotonics: ferroelectric $BaTiO_3$ devices, Nano Lett. 14 (3) (2014) 1419–1425. Available from: https://doi.org/10.1021/nl404513p.
[190] S. Abel et al., "Barium Titanate Thin Films Embedded in Silicon Photonic Structures for Ultra-Efficient Electro-Optical Tuning," Sep. 2016. Available from: https://doi.org/10.7567/SSDM.2016.C-5-01.
[191] F. Eltes, et al., Low-loss $BaTiO_3$–Si waveguides for nonlinear integrated photonics, ACS Photonics 3 (9) (2016) 1698–1703. Available from: https://doi.org/10.1021/acsphotonics.6b00350.
[192] F. Eltes, et al., An integrated optical modulator operating at cryogenic temperatures, Nat. Mater. 19 (11) (2020) 1164–1168. Available from: https://doi.org/10.1038/s41563-020-0725-5.
[193] F. Eltes, et al., A $BaTiO_3$-based electro-optic Pockels modulator monolithically integrated on an advanced silicon photonics platform, J. Light. Technol. 37 (5) (2019) 1456–1462. Available from: https://doi.org/10.1109/JLT.2019.2893500.
[194] <http://www.lumiphase.com>.
[195] S. Abel, D.J. Stark, F. Eltes, J.E. Ortmann, D. Caimi, J. Fompeyrine, "Multi-level optical weights in integrated circuits," in: 2017 *IEEE International Conference on Rebooting Computing (ICRC)*, Nov. 2017, pp. 1–3. Available from: https://doi.org/10.1109/ICRC.2017.81236722.
[196] A. Messner, et al., Plasmonic ferroelectric modulators, J. Light. Technol. 37 (2) (2019) 281–290. Available from: https://doi.org/10.1109/JLT.2018.2881332.
[197] J.E. Ortmann, et al., Ultra-low-power tuning in hybrid barium titanate–silicon nitride electro-optic devices on silicon, ACS Photonics 6 (11) (2019) 2677–2684. Available from: https://doi.org/10.1021/acsphotonics.9b00558.